Colloids and Surfaces A: Physicochemical and Engineering Aspects 625 (2021) 126857

Contents lists available at ScienceDirect

Colloids and Surfaces A: Physicochemical and Engineering Aspects

journal homepage: www.elsevier.com/locate/colsurfa

Surfactant inhibition mechanisms of carbonate mineral dissolution in shale

Kyung Tae Kim [a], Mantha Sai Pavan Jagannath [c], Gregory M. Su [d,e], Guillaume Freychet [f], Tongzhou Zeng [b], Kishore K. Mohanty [b], Graeme Henkelman [c], Lynn E. Katz [a], Charles J. Werth [a,*]

[a] Department of Civil, Architecture & Environmental Engineering, University of Texas at Austin, 301 East Dean Keeton St., Austin, TX 78721, USA
[b] Hildebrand Department of Petroleum & Geosystems Engineering, University of Texas at Austin, 200 East Dean Keeton St., Austin, TX 78721, USA
[c] Department of Chemistry, University of Texas at Austin, 2506 Speedway Dr., Austin, TX 78721, USA
[d] Advanced Light Sources, Lawrence Berkeley National Laboratory, Berkeley, CA 94720, USA
[e] Materials Sciences Division, Lawrence Berkeley National Laboratory, Berkeley, CA 94720, USA
[f] National Synchrotron Light Source II, Brookhaven National Laboratory, Upton, NY 11973, USA

GRAPHICAL ABSTRACT

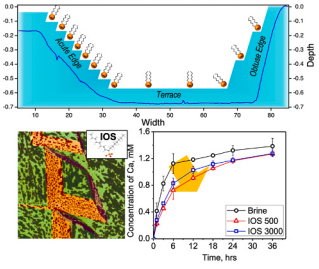

ARTICLE INFO

Keywords:
Eagle Ford shale
Calcite
Anionic surfactant
Density functional theory
Time of flight secondary ion mass spectrometry
Near edge X-ray absorption fine structure spectroscopy

ABSTRACT

Surfactants are common additives to hydraulic fracturing and enhanced oil recovery (EOR) fluids, and are under consideration for amendment to supercritical carbon dioxide for geological carbon sequestration (GCS). The effect of a common anionic surfactant, internal olefin sulfonate (IOS), on mineral dissolution from shale into brine was evaluated. When added to brine at concentrations exceeding the critical micelle concentration (94 mg/L), IOS inhibited carbonate mineral dissolution in an Eagle Ford shale, as well as dissolution of optical quality calcite (the dominant carbonate in the shale). Laser profilometry images provide spatial resolution across > 3 orders of magnitude, and indicate that IOS addition to brine both enhances the formation of new etch pits in calcite, and impedes their further growth. Time-of-flight secondary ion mass spectrometry surface profiles show for the first time that IOS preferentially adsorbs at calcite pit edges versus flat calcite surfaces (i.e., terraces). Surface pressure calculations, sulfur K-edge near edge X-ray absorption fine structure (NEXAFS) spectroscopy results, and density functional theory (DFT) calculations support this observation; the DFT results indicate that the sulfonate head group of the IOS molecule binds strongly to the calcite step site as compared to the terrace site. The S K-edge NEXAFS results indicate that IOS adsorbed more to etched calcite surfaces compared to smooth calcite surfaces. Overall, the results indicate that weak adsorption on flat calcite surfaces (i.e., terraces) disrupts water structure and enhances mass transfer of dissolution, while strong adsorption on calcite pit edges displaces adsorbed water and inhibits further etch pit growth. This work provides the first direct evidence of preferential

* Corresponding author.
E-mail address: werth@utexas.edu (C.J. Werth).

https://doi.org/10.1016/j.colsurfa.2021.126857
Received 1 March 2021; Received in revised form 13 May 2021; Accepted 14 May 2021
Available online 19 May 2021

adsorption of IOS to etched calcite surfaces and links it to macroscopic dissolution kinetics. This work has implications for surfactant-containing fluids used in hydraulic fracturing, EOR and potentially GCS for subsurface injection into carbonate rich reservoirs.

1. Introduction

Shale formations have emerged as critical stratigraphic units in unconventional hydrocarbon recovery [1,2] and geological carbon sequestration [3,4]. In the former they are rich sources of oil and natural gas, and in the latter they serve as cap rock to prevent carbon dioxide escape. Shales are complex assemblages of fine mineral fragments and organic matter of varying reactivity [5], and in many cases are dominated by highly reactive carbonate minerals (e.g., Eagle Ford shale > 60% calcite [6–8], Wolfcamp and Marcellus shales > 80% calcite + dolomite). Shales are exposed to injected fluids during hydraulic fracturing and geological carbon sequestration leading to dissolution and secondary mineral precipitation. Dissolution has been shown to open pore spaces and fractures in shale matrices and create conduits for fluid flow [9,10], and to decrease geomechanical integrity [10,11]. The latter can weaken rock, promoting collapse as rubble and the closure of propped fractures, or promote slippage along grain and fracture boundaries inducing seismicity. A number of researchers have investigated the effects of water with varying pH, carbon dioxide partial pressure (pCO_2), and temperature on shale mineral reactions [3,9,12]. The effects of various additives have also been evaluated [13,14]. However, the effects of surfactants on mineral reactivity have rarely been addressed.

Surfactants are commonly added to hydraulic fracturing and enhanced oil recovery (EOR) fluids to reduce interfacial tension and to alter reservoir wettability [16,17]. Anionic, cationic, zwitterionic, and nonionic surfactants are all used in practice, and the type selected for use in a reservoir depends on many factors including formation mineralogy, salinity, hardness, pH, and temperature [18]. Surfactant head groups bind to oppositely charged sites on mineral surfaces via electrostatic forces, and this is aided by weaker van der Waal forces [19,20]; this is also aided by favorable entropy changes that occur when hydrophobic surfactant tails partition from brine to neutrally charged mineral surfaces and natural organic matter. Near neutral pH, carbonates (e.g., points of zero $charge_{calcite}$ = 8–9.5 [21]) are positive and this aids anionic surfactant sorption [22]. At low concentrations on mineral surfaces, individual and non-interacting surfactant molecules adsorb at the most favorable sites (e.g., edges) [23,24]. As concentrations increase, hemimicelles can form at these same sites, and at less favorable sites, and surfactant molecules can interact with each other. Above the critical micelle concentration (CMC), adsorption is independent of surfactant concentration. Surfactants have been used to protect metal surfaces from corrosion in acidic solutions, with the assumption that they inhibit proton attack [25]. It follows that surfactants might protect shale mineral surfaces from dissolution, but this has not been examined.

The ubiquity of carbonates in shales and other human-impacted systems (e.g., conventional reservoirs, potable groundwater aquifers, soil, biological systems, and engineered structures) has motivated study of their reactivity under widely varying conditions [26,27]. Among the most studied carbonate is calcite, and its dissolution is of interest in this study. Broadly, calcite dissolution occurs by surface etching, where bound calcium and carbonate ions are solubilized on calcite surfaces preferentially at defect sites such as step edges and edge kinks [28–31]. Various rate laws and mechanisms have been proposed to describe calcite dissolution rates. In relatively pure water, dissolution rates have been related to proton (a_{H^+}), carbon dioxide ($a_{H_2CO_3^*}$), water (a_{H_2O}), calcium ($a_{Ca^{2+}}$), and bicarbonate ($a_{HCO_3^-}$) activities via Eq. (1) [32].

$$R = k_1 a_{H^+} + k_2 a_{H_2CO_3^*} + k_3 a_{H_2O} - k_4 a_{Ca^{2+}} a_{HCO_3^-} \quad (1)$$

where $[H_2CO_3^*] = ([CO_2(aq)] + [H_2CO_3^\circ])$. Below ~ pH 3.5 the first term on the right hand side of Eq. (1) dominates. At higher pH, the forward reaction is governed by the second and/or third term depending on pCO_2 and pH. The reverse (precipitation) reaction (fourth term) becomes important as the solution approaches saturation with respect to calcite. When the third term dominates, dissolution is sufficiently slow such that mass transfer to the calcite surface can be ignored.

Many studies have evaluated the effects of aqueous constituents on calcite growth and dissolution, with the greater focus on inorganic ions. Both inhibition (e.g., organic acids, Fe^{2+}, Mg^{2+}, Sr^{2+}, PO_4^{3-}) and enhancement (e.g. chelators, Cl^-, I^-, F^-,) of dissolution kinetics have been observed [33–42], and in some cases enhancement changed to inhibition or vice versa as the concentration and/or molecular weight of structurally similar molecules changed (e.g., polyaspartate) [43,44]. Inhibition kinetic effects are often attributed to ion adsorption and pinning at step edges [33], as well as general competitive adsorption with Ca^{2+} and/or CO_3^{2-} [35]. Inhibition has also been related to incorporation of metal impurities into the carbonate mineral [36,45]. Enhancement of the kinetics is less common, but has been attributed to disruption of the adsorbed water layer at the calcite surface with possible lowering of the energy barrier for etch pit nucleation and enhanced mass transfer [43,44,46].

Aqueous constituents also affect calcite etch pit geometry. Rhombohedral etch pits ideally form on $\{10\bar{1}4\}$ surfaces in pure water. These pits primarily grow by dissolution of Ca^{2+} and CO_3^{2-} along acute and obtuse edges, and growth along obtuse steps is faster in pure water [28]. Inorganic ions have been shown to favorably adsorb at acute or obtuse edges, and thereby promote growth of etch pits in one or the other direction [33,36]. The effects of adsorbed organic ions appear even more complex and have been extensively studied in the field of biomineralization. Organic molecules containing amino acid or carboxyl groups bind with calcite surface and step edges by stereochemical recognition, resulting in macroscopic etch pit morphology modification or stabilization of different crystal facets [30,43,47–49]. Poly-n-aspartic acid, for example, was shown to preferentially adsorb to acute edges for n = 1, 2, and obtuse edges for n = 3, 4, 6 [43], thereby promoting growth in opposite directions. Also, different enantiomers of aspartic acid (i.e., D- and L-) adsorb at opposite acute edges of etch pits and yield different mirror image etch pit geometries [30]. The effects of surfactants, which have different hydrophilic functional groups (e.g. sulfonate) that can potentially interact with mineral surfaces and also hydrophobic chains that induce complex adsorption behavior by forming micelles, on calcite dissolution rates and etch pit morphologies have received little attention.

The objectives of this study are to determine which component(s) of shale are most reactive with a simplified model brine (0.4 M KCl) at circumneutral pH and low total carbonate (C_T) under ambient pCO_2, whether an anionic surfactant protects shale mineral component(s) from dissolution, and to identify the mechanisms of this protection. To address these objectives, dissolution kinetics of an Eagle Ford shale were measured under ambient conditions in brine without and with the anionic surfactant internal olefin sulfonate (IOS). Dissolution results and geochemical modeling were used to identify which mineral(s) reacted and were protected by IOS. Calcite was identified as the primary mineral protected by IOS from dissolution, and the dissolution kinetics of optical quality calcite were similarly measured and complemented with laser profilometry images of resulting etch pit geometries. Calcite-brine surface pressure values were determined from wettability measurements. Site specific distribution of IOS on calcite surfaces was evaluated with time-of-flight secondary ion mass spectrometry (ToF-SIMS), and further

probed with near edge X-ray absorption fine structure (NEXAFS) spectroscopy and density functional theory (DFT) calculations. These different methods provided multiple lines of evidence to interpret the mechanisms affecting calcite dissolution inhibition by IOS.

2. Experimental

2.1. Materials

Most stock chemicals received were reagent grade. They include 1 M HCl (Aldrich® 99.99%), HNO_3 (Fisher, Trace metal grade), 1 N KOH (J. T.Backer, analytical grade), and solid KCl (Aldrich®, 99%). A 30.1 wt% anionic surfactant solution of internal olefin sulfonate (IOS C15-18), hereafter refered to as IOS, was obtained from Shell Oil Company (product number O332); a representative structure of IOS is shown in Fig. 1a. A core sample of oil-wet shale from a burial depth of 3400 m was obtained from the Eagle Ford reservoir in south Texas. Optical quality calcite crystals from Brazil and gypsum crystals were purchased from Ward's Scientific. Ultrapure water was prepared from a Thermo Scientific Barnstead Nanopure Model 7143, and it was characterized by a resistivity of 18.2 MΩ cm.

2.2. Brine and IOS brine solution preparation

Ultrapure water and powdered KCl were combined to make a 0.401 M KCl solution, hereafter referred to as brine solution. This corresponds to an ionic strength of 0.401 M, which is similar to lower values identified in Eagle Ford shale formation water [50]. The anionic IOS surfactant was received and stored in a highly basic stock solution to maintain compound stability. It was chosen because it is a common additive to both enhanced oil recovery and hydraulic fracturing fluids [51,52]. The key roles of surfactants in hydraulic fracturing and EOR are interfacial tension reduction and reservoir wettability alteration to a more water-wet state [53]. Just before use, the required amount of IOS stock solution was diluted to 15,000 mg/L, then mixed with HCl to adjust the pH to 4.3. This pH reduction transformed all carbonate species into carbonic acid (H_2CO_3*). Subsequently, sonication and vacuum were applied to degas dissolved CO_2 until no gas evolution was apparent. The pH of this solution was then adjusted upward to > 6 by adding 0.1 M KOH. The CO_2 removal by sonication and vacuum was confirmed by acid titration with HCl. The pH-adjusted IOS stock solution was then diluted into brine to obtain desired IOS concentrations (e.g., 500 mg/L and 3000 mg/L). The pH values of all brine and combined IOS brine solutions were adjusted to 6.3 using 0.1 M HCl before use.

2.3. Eagle Ford shale and calcite sample preparation

The Eagle Ford shale was used in powder form. Larger chunks of Eagle Ford shale were turned into powder by grinding with a mortar and pestle. This powder was then rinsed in brine three times by sequential centrifugation at 6000 rpm and decanting; this was done to remove very fine mineral and organic matter particles that could pass through a syringe polyethersulfone (PES) filter during experimental sampling (see next section). The decanted brine was discarded, and the retained solids ($> 98\%$) were dried and then used in experiments.

The optical quality calcite was used as coarse grain particles, and in cleaved samples. Coarse grain particles were created by first rough grinding using a mortar and pestle. Next, these particles were passed through a #20 mesh sieve, and then collected on a #100 mesh sieve, to obtain the desired size fraction (150–850 μm). These calcite particles were then quickly (minutes) rinsed by sonicating in ultrapure water and decanted to remove very fine particles. Cleaved samples were prepared by cleaving 2 mm thick by ~ 1 cm^2 calcite specimens from larger blocks of optical quality calcite using a razor [54]. The cleaving exposed fresh $\{10\bar{1}4\}$ surfaces, and the cleaved samples were immediately immersed in experimental solution (details below) to prevent surface contamination and reaction with the atmosphere.

2.4. Eagle Ford shale and calcite dissolution experiments

Eagle Ford shale batch dissolution experiments were performed in 40 mL vials at 22 ± 1 °C by submerging ~ 0.5 g of powered samples in 10 mL of brine alone or IOS mixed brine solutions (hereafter referred to as IOS brine), and then sampling and analyzing for dissolved elements and ions over time. The vials were loosely covered so that CO_2 could exchange between brine and the atmosphere (open system), and then mixed with a stir bar. In most experiments, ~ 0.3 mL brine samples were collected at 1, 3, 6, 12, and 48 h. All aqueous samples were collected through a 0.22 μm syringe filter.

Calcite batch dissolution experiments were performed in 40 mL vials at 22 ± 1 °C by submerging ~ 0.5 g of particles or cleaved samples in 10 mL of brine alone or IOS brine, and then sampling and analyzing for Ca^{2+}, pH, and total carbonate over time. As before, the vials were loosely covered so that CO_2 could exchange between brine and the atmosphere, and for calcite particles the solution was continuously mixed. For all experiments, approximately 0.3 mL samples were collected after 1, 3, 6, 12, and 36 h, again through 0.22 μm PES filters.

Calcite etch-pit experiments were performed using only cleaved calcite pieces. In one set of experiments, the cleaved calcite pieces were submerged in brine alone or IOS brine for 12 h, removed from solution and gently rinsed with ethanol to remove salts and adsorbed IOS, dried

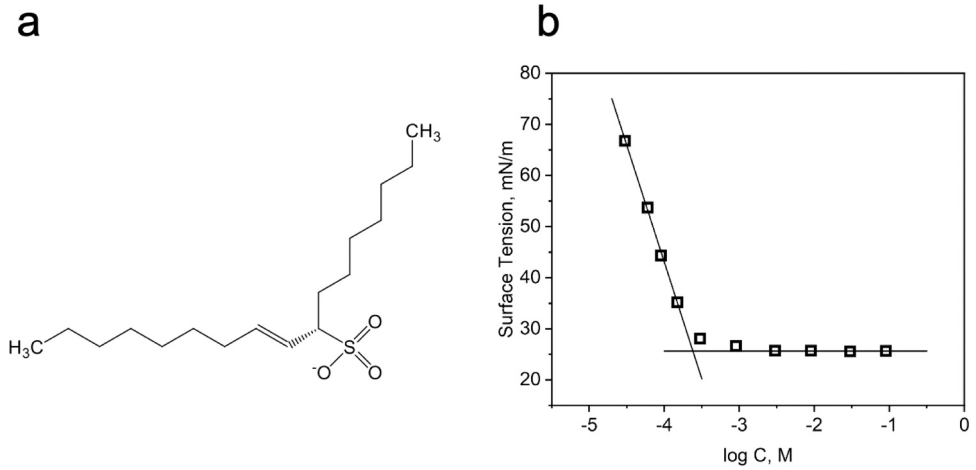

Fig. 1. a) Representative structure of IOS (C17), b) surface tension as a function of log molar concentration of IOS in brine (0.401 M KCl) at room temperature.

with pure N_2, and then analyzed using laser profilometry. In another set of experiments, replicate calcite samples submerged in brine for 12 h were then subsequently transferred to either a solution of only brine or a solution of IOS brine for another 12 h. After this second aging period, the samples were again rinsed with ethanol, dried with N_2. After each aging steps, the samples were evaluated using laser profilometry to track etch pit growth.

All experiments were performed under ambient conditions, while reservoirs are typically under high pressure and elevated temperature. Hence, this work represents a first step toward mechanistic evaluation of surfactant effects on shale mineral dissolution, and further work under reservoir conditions is warranted.

2.5. Measurement of Ca^{2+} in ion exchange sites

The cation exchange capacity was measured following the method proposed by Amrhein and Suarez which is pertinent for calcite and/or gypsum rich soils [55]. Also, the amount of Ca^{2+} in ion exchange sites at the start of Eagle Ford shale dissolution experiments was evaluated to distinguish this contribution from dissolution of calcium-containing minerals. Briefly, powdered Eagle Ford shale samples were rinsed three times in brine and then placed into a 0.5 M aqueous solution of $MgCl_2$. The Ca^{2+} in solution was then measured. The Mg^{2+} will displace Ca^{2+} from cation exchange sites, as well as promote mineral dissolution because it is under-saturated in calcium. The Ca^{2+} displaced by Mg^{2+} is distinguished by subtracting the concentration of constituent ions (e.g., CO_3^{2-} for calcite, SO_4^{2-} for gypsum) from the measured total Ca^{2+} concentration.

2.6. Surface tension and contact angle measurements

A Ramé-hart Model 500 Goniometer was used for surface tension and contact angle measurements. Surface tension values were determined for brine and mixtures of IOS and brine using the pendant drop method. The CMC of IOS also was determined by calculating an inflection point from the surface tension vs log IOS concentration plot (Fig. 1b). Contact angle values for brine and IOS brine were determined by placing a drop of these liquids onto a freshly cleaved or aged calcite surface, and measuring contact angles from image analysis. The calcite surface was washed between measurements following Costa and Aquilano [56]. Each surface tension and contact angle value reported is the average of five different measurements.

2.7. Elemental and ion analyses

Elemental analysis was performed using a Varian 710-ES inductively coupled plasma – optical emissions spectroscopy (ICP-OES) instrument. Lower detection limits for Ca and Mg are 0.03 μg/L and 0.1 μg/L, respectively. 100 μL of each sample collected from experimental vials was diluted into 9.9 mL of Nanpure water mixed with 200 μL of concentrated nitric acid, and then analyzed for Ca and Mg. The oxyanion sulfate (SO_4^{2-}) was measured using a Thermo scientific Dionex ICS-2100 ion chromatograph (IC). 50 μL of each sample collected from experimental vials was diluted into 0.95 mL of ultrapure water and analyzed. Solution pH was measured using a Mettler Toledo pH electrode LE438. Carbonates were measured by acid titration using HCl.

2.8. Surface area, mineralogy, and total organic carbon

The specific surface area (SSA) of Eagle Ford shale was measured using N_2 adsorption with a Micromeritics 3Flex Surface Area analyzer. Samples were analyzed over the pressure range from 0.73 to 748 mm Hg at 77 K, and analyzed using the Brunauer–Emmett–Teller isotherm. Mineralogy and total organic carbon (TOC) of the Eagle Ford shale were measured by the commercial laboratory, Premier Oilfield Group. The former was measured by X-ray diffraction (XRD) using a Bruker D8 diffractometer, and the later by a total organic carbon analyzer using a Leco-carbon analyzer.

2.9. Laser profilometer analysis

A Keyence VK-1100 Laser Profilometer was used to characterize surface morphology and pit formation. Surface profiles were mainly collected with 50× lens to scan 211 × 281 μm^2. The vertical display resolution is 0.5 nm, and the precision of repeated scans in the laser confocal mode with the 20× lens is 40 nm. Depending on the size of the pits, higher magnification lenses were used. Surface profiles were processed with VK-X series Multi-file Analyzer software. The reference plain setting was first performed with a relatively flat surface, and then the depth and area of each pit were measured by referencing the adjacent flat surface. The arithmetic average areal roughness (S_a) was calculated over the scanned area.

2.10. IOS surface location and coverage on calcite

IOS surface location and coverage on calcite pieces were determined using Time-of-Flight Secondary Ion Mass spectrometry (ToF-SIMS). Freshly cleaved calcite samples were aged in brine for 12 h to form etch pits. The brine was then mixed with IOS to reach 10 or 100 mg/L, and allowed to incubate for 1 h. Samples were then removed from solution, gently dried by blowing ultrapure N_2, and placed in the ToF-SIMS instrument for analysis of the spatial distribution of IOS (i.e., SO_2^-) and calcite (i.e., Ca^-, CO_3^-) containing molecular fragments. A calcite sample aged in brine without IOS and a drop of concentrated IOS (30.1 wt%) on a silicon wafer were also analyzed as controls.

The specific instrument used was an ION-TOF (GmbH, Germany, 2010). During the sputtering/analysis process, a Cs^+ sputtering ion beam (beam energy 500 eV, current ~ 40 nA), and a pulsed Bi_3^+ cluster analysis ion beam (30 keV ion energy, 100 ns pulse duration) with either 3.7 pA (depth profiling) or 2.7 pA (high-resolution imaging) of measured sample current, were used. Additional details are in Supporting information.

Relative amounts of IOS adsorbed on calcite with and without etch pits were determined using near edge X-ray absorption fine structure (NEXAFS) spectroscopy. A freshly cleaved gypsum ($CaSO_4{\cdot}2H_2O$) and concentrated IOS (30.1 wt%) on a silicon wafer were prepared as controls to determine energy shift correction and type of sulfur functional groups in the IOS. A freshly cleaved calcite was also analyzed as a control to investigate sulfur impurities. Four additional samples with two different surface morphologies (i.e., etched or cleaved calcite) were prepared by first aging cleaved calcite in brine or calcite saturated brine, respectively for 12 h. The brine or calcite-saturated brine was then mixed with IOS to reach 10 or 100 mg/L, and allowed to incubate with the calcite samples for 1 h. The calcite-saturated brine was used to prevent etch pit formation and to hydrate calcite surface prior to adding IOS. Samples were then collected and dried following the procedure described with samples for ToF-SIMS. All calcite samples were prepared by cleaving a single calcite crystal.

NEXAFS measurements were performed at beamline 12-ID at the National Synchrotron Light Source II (NSLS-II). Fluorescence-yield (FY) NEXAFS data were collected near the sulfur K-edge (2449–2504 eV) and calcium K-edge (4030–4110 eV) using a Pilatus 300 KW detector positioned at 0.7° from the sample plane for both sulfur K-edge and calcium K-edge measurements. The total intensity from a region of the detector away from any scattering peaks was used as a fluorescence signal. Pre-edge subtraction and post-edge normalization was performed with Larch software [57]. Subsequently, normalized spectra were decomposed using multipeak fitting package 2 in Igor pro (WaveMetrics). Each spectrum was decomposed into 5 or less Gaussian functions and an arctangent function following the approach proposed by Manceau and Nagy [58].

2.11. Geochemical modeling

Geochemical modeling was performed using PHREEQC. The *phreeqc.dat* database was used for thermodynamic data [59]. A list of reactions considered is in Table S1 (Supporting information). The model was run by first defining the composition of brine in equilibrium with atmospheric CO_2 at 22 °C, and then equilibrating that solution with calcite and other Ca bearing minerals in the Eagle Ford shale (i.e., dolomite, gypsum). The moles of added minerals and the volume of solution were specified based on measured solution species and experimental conditions. Additional details are in Section 3.3.

2.12. Density functional theory calculations

Density Functional Theory (DFT) calculations based on the Generalized Gradient Approximation (GGA) were performed using the Vienna Ab initio Simulation Package (VASP). A plane wave basis set was used with an energy cutoff of 300 eV and a Gaussian smearing at the Fermi level with a width of 0.05 eV to improve convergence. The Perdew–Burke–Ernzerhof (PBE) [64] functional was used to describe electron exchange and correlation. The Brillouin zone was sampled at the Γ-point. The convergence criteria for electronic and geometric optimization were 10^{-6} eV and 0.01 eV/Å, respectively.

To mimic the experimental surfaces, slab models of calcite $\{10\bar{1}4\}$ were constructed with the atoms in the bottom layer fixed in bulk positions. The thickness of the vacuum layer was set to 14 Å to isolate the periodic slabs. Our model of the IOS molecule had 10 carbon atoms in the hydrocarbon side chains. The binding energy of the IOS molecule to the calcite substrate was calculated as

$$E_{binding} = E_{surface-IOS} - E_{surface} - E_{IOS} \quad (2)$$

where $E_{surface}$ is the energy of the calcite surface, E_{IOS} is the energy of isolated IOS molecule and $E_{surface\text{-}IOS}$ is the energy of the system when IOS binds to the calcite surface. The VASPsol code [65] was used to consider (implicit) solvent interactions as a continuum dielectric with a relative permittivity set to 78.4 to mimic water.

3. Results and discussion

3.1. Sample characterization results

The measured SSA of Eagle Ford shale is 6.65 ± 0.05 m^2/g. These results are consistent with SSA measurements in the literature for Eagle Ford shale [7]. Mineralogical results for our Eagle Ford shale are shown in Table 1. They show that the sample is comprised of 67% calcite, 8.7% quartz, 6.2% Illite and Mica, 4.2% Illite/Smectite mixture, 5% K-feldspar, 4.1% plagioclase, and minor amounts of pyrite, kaolinite, chlorite, apatite, and siderite. This composition is similar to that measured by others [6–8], except for the lack of small amounts of gypsum and dolomite.

Table 1
Mineralogy and total organic matter content of Eagle Ford shale sample.

Mineral	Chemical formula	Eagle Ford Shale
Calcite	$CaCO_3$	67.5%
Dolomite	$CaMg(CO_3)_2$	0%
Siderite	$FeCO_3$	0.2%
Apatite	$Ca_5(PO_4)_3OH$	0.7%
Pyrite	FeS_2	1.3%
Quartz	SiO_2	8.7%
K-Feldspar	$KAlSi_3O_8$	5.0%
Plagioclase	$NaAlSi_3O_8$-$CaAl_2Si_2O_8$	4.1%
Total Clays	Clay constituents below	11.6%
Chlorite		0.5%
Kaolinite		0.7%
Illite/Mica		6.2%
Mixed Illite/Smectite		4.2%
Total Organic Carbon		3.7 mg/g

The cation exchange capacity of the Eagle Ford shale is 89.1 meq/kg. The Ca and alkalinity (HCO_3^-) released into brine by Eagle Ford shale upon exposure to 0.5 M $MgCl_2$ after rinsing three times in brine were also measured. The difference between measured Ca and alkalinity was less than 0.01 mM. This indicates that at the start of Eagle Ford shale dissolution experiments (next section) there was no Ca^{2+} available for release from cation exchange sites. Any Ca^{2+} initially present at these sites was exchanged and removed during the triplicate KCl rinsing steps. Therefore, any Ca^{2+} released during Eagle Ford shale dissolution experiments is likely due to mineral dissolution.

Surface tension and contact angle results for calcite sample are presented in Table 2. The surface tension decreases when IOS is added to the brine, and there is no difference for the two IOS concentrations (which are both above the critical micelle concentration (CMC) of 94 mg/L). Contact angles on freshly cleaved calcite decrease with IOS addition to brine. The same measurements were taken on calcite after it was aged 12 h in brine to create etch pits, and contact angles were lower for all cases. Calcite-brine interfacial tension values were calculated from Young's equation [60]; similar values were obtained for all setups (438 mJ/m^2 to 443 mJ/m^2) except a lower value was obtained for aged calcite with brine only (411 mJ/m^2). By comparison, Costa and Aquilano determined a comparable value of 409 mJ/m^2 for calcite and fresh water [56]. Aging calcite increases surface roughness (Section 3.5), which can further decrease interfacial tension [61,62]. Costa and Aquilano allowed their sample to "equilibrate in air", which may have increased surface roughness. Surface pressures (F) at the calcite-brine interface resulting from IOS addition were calculated from differences in interfacial tension ($F = \gamma_{SL(IOSBrine),i} - \gamma_{SL(Brine),i}$, where i is for fresh or aged calcite) following Fowkes and Harkins [63]. Values for fresh calcite were very small and not distinguishable from zero, while values for aged calcite were relatively large; the results indicate that the IOS preferentially adsorbs on aged versus fresh calcite-water interfaces.

3.2. Dissolution of Eagle Ford shale

Dissolution experiments were performed for Eagle Ford shale over a 48 h period in brine and IOS brine. Results for the first 12 h are shown in Fig. 2, and for the entire 48 h period in Fig. S1 (Supporting information). At the two IOS concentrations used (i.e., 500 and 3000 mg/L), approximately 61% (6.1 mg/g) and 12% (6.9 mg/g) of the IOS masses added to solution adsorbed to shale components, respectively, based on measured adsorption isotherms [64]. Total surface area covered by adsorbed molecules was estimated using the minimum surface area per molecule calculated from the Gibbs equation [65], i.e., 20.7 $Å^2$. Detailed calculations are in the Supporting information. The total surface area covered by IOS at 500 and 3000 mg/L are 34.6% and 39.0% of the measured surface areas using N_2 adsorption, respectively. Also, IOS concentrations in solutions (i.e., 194 mg/L and 2655 mg/L) after sorption at both loadings exceed the CMC (94 mg/L). The elements Ca, Mg, Fe, S, Al, and Si were initially monitored in solution, and only Ca, Mg, and S appreciably changed. For S, the sulfate ion (SO_4^{2-}) was measured using ion chromatography and is reported in this form.

Per Fig. 2, the concentrations of Ca, Mg, and SO_4^{2-} all increased during the monitoring period, and an initial rapid rise is followed by a decreasing rate of increase; the pH during this time increases from 6.3 to approximately 8.0. This initial high rate of dissolution is expected, as fresh brine solution contains very few mineral species (e.g., no Ca, Mg, SO_4^{2-}, and only low CO_3^{2-}) and the driving force for dissolution is large. Over time, these species build up and mineral dissolution slows, but does not appear to reach steady state after 48 h. The Ca concentrations at 48 h are approximately 15–41 times greater than the SO_4^{2-} or Mg concentrations, respectively. Per XRD, the only Ca containing mineral measured was calcite. However, the presence of Mg and SO_4^{2-} indicates

Table 2
Contact angles, interfacial tensions, and adsorbed IOS.

Parameter	Brine		IOS 500		IOS 3000	
	Fresh	Aged	Fresh	Aged	Fresh	Aged
Brine-Calcite Contact Angle[a]	72.9 ± 5.4°	42.5 ± 10.5	38.8 ± 4.0°	22.5 ± 3.8	20.5 ± 1.9°	10.7 ± 2.2
Brine-Air Surface Tension [mJ/m^2][b]	71.9 ± 0.4		28.1 ± 0.9		26.6 ± 0.01	
Brine-Calcite Interfacial Tension [mJ/m^2][c]	443	411	442	438	439	438
Surface Pressure [mJ/m^2][d]	NA	NA	−0.9[e]	27	−0.2[e]	27

[a] The left and right sides of five drops on calcite were evaluated for each measurements.
[b] Pendant drop method.
[c] Based on Young's relation ($\gamma_{LV}\cos\theta = \gamma_{SV} - \gamma_{SL}$). The surface tension of calcite with air is 464 mJ/m^2 from Bruno et al. [83].
[d] From Fowkes and Harkins [63] ($F = \gamma_{LV,IOSBrine}\cos\theta_{IOSBrine} - \gamma_{LV,Brine}\cos\theta_{Brine}$).
[e] These values result from subtracting one large number from another, and are not significantly different from zero. Therefore, these two surface pressures are too small for accurate quantification.

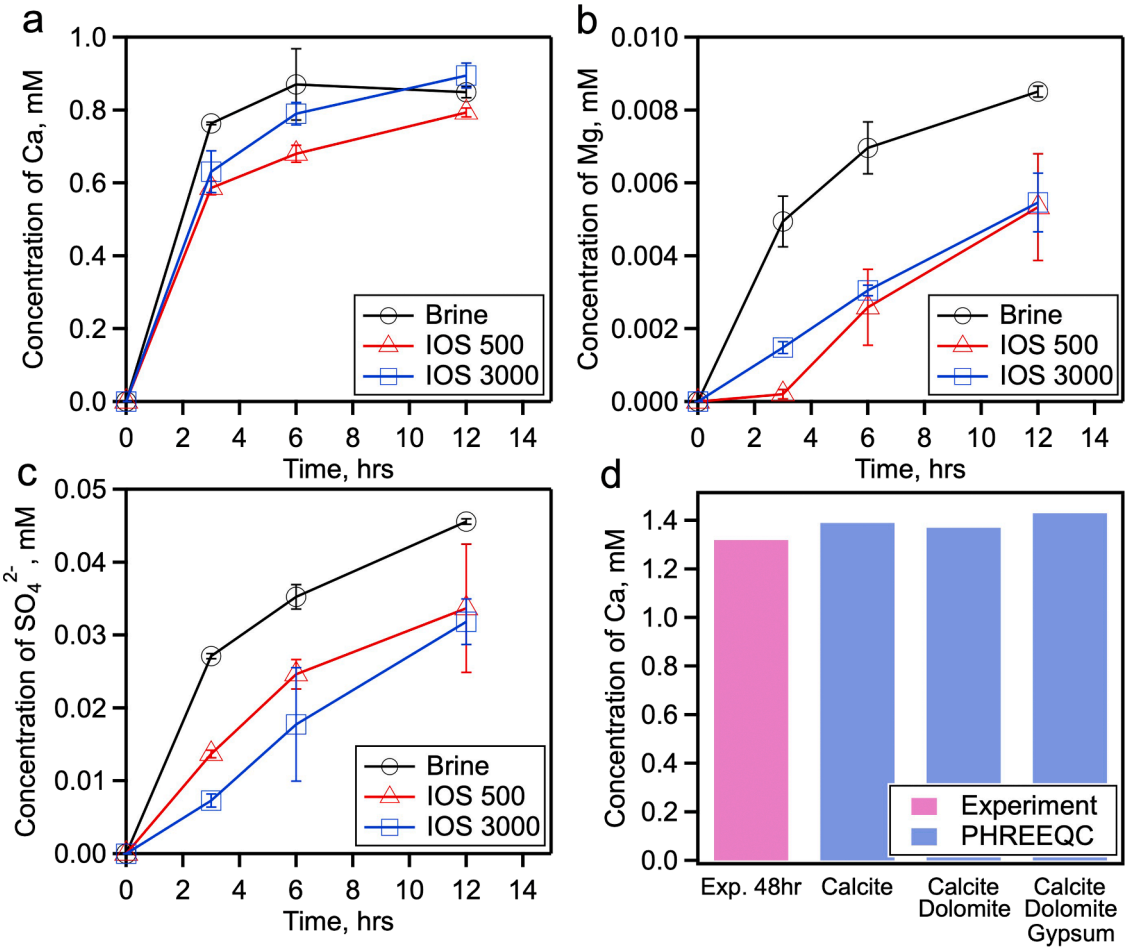

Fig. 2. a) Ca, b) Mg, and c) SO_4^{2-} release into solution from Eagle Ford Shale after aging in brine or IOS brine for 12 h. Initial pH of the solution is 6.3, and ionic strength of brine is 0.4 M. All experiments were run in triplicate, and error bar represents standard deviation. d) PHREEQC modeling results showing potential mineral contributions to Ca concentrations. IOS 500 and IOS 3000 refer to brine with either 500 or 3000 mg/L of IOS added.

minor amounts of dolomite and gypsum are present, and they have been identified in other samples of Eagle Ford shale [6–8].

Also per Fig. 2, Ca, Mg, and SO_4^{2-} concentrations in brine and IOS brine are different. For Ca, this difference is only significant at 3 h, and then it becomes indistinguishable with respect to the measurement error. However, for Mg and SO_4^{2-} the differences persist over 48 h, but the magnitudes of these differences are small compared to those for Ca at 3 h. Results for the different IOS concentrations are not as consistent. For example, less Ca dissolves for IOS 500 compared to IOS 3000, whereas for SO_4^{2-} the opposite is true. The reason for the conflicting trends is not clear, and may be due to transient uptake of IOS and/or inorganic ions onto ion exchange sites and/or hydrophobic domains in organic matter. Regardless, these results indicate that IOS protects shale minerals from dissolution. They also indicate that IOS primarily protects calcite from dissolution in the Eagle Ford shale but this effect is transient.

The pH and total carbonate were monitored during Eagle Ford shale dissolution and (along with ionic strength) used to calculate ion activities (i.e., a_{H^+}, $a_{H_2CO_3^*}$, a_{H_2O}, $a_{Ca^{2+}}$, $a_{HCO_3^-}$) using PHREEQC. These were used with calculated rate constants from Plummer et al. [32] to approximate which terms in Eq. (1) dominate calcite dissolution from the shale. At time zero to 12 h, $k_3 a_{H_2O}$ dominates Eq. (1), and the contribution of $k_4 a_{Ca^{2+}} a_{HCO_3^-}$ to Eq. (1) increases with time (Table S3). At

48 h, $k_4 a_{Ca^{2+}} a_{HCO_3^-}$ slightly exceeds $k_3 a_{H_2O}$. However, the saturation index (SI) for calcite remains below 0 at all times, indicating only dissolution and not precipitation is active.

3.3. Ca^{2+} mass balance in Eagle Ford shale

PHREEQC modeling was performed to determine if the Ca measured in brine solution during Eagle Ford shale dissolution at 48 h was near equilibrium with calcite, and/or if other unaccounted sources of Ca were present. Modeling results are presented in Fig. 2d; model equations are presented in Table S1 (Supporting information). Only minerals containing Ca, Mg, CO_3^{2-}, and SO_4^{2-} were considered, since only these were identified in brine. Three different mineral phases were defined in modeling. Calcite was defined as an infinite mineral, since 67.5% of Eagle Ford shale is calcite. Dolomite and gypsum were also considered sources of Ca, and the moles of these minerals were set equal to the moles of Mg and SO_4^{2-} in solution at 48 h, respectively. Alkalinity and pH were measured at 48 h and were used to determine pCO_2. Finally, modeled pH, alkalinity, Mg, and SO_4^{2-} were compared with measured values for validation. The measured Ca concentration in solution after 48 h represents the baseline for comparison.

Results in Fig. 2d show that the measured Ca in solution is approximately 95.5% of the theoretical value at equilibrium. The contributions from dolomite and gypsum to modeled total Ca are 2.2% and 6.6% of total Ca, respectively, with the remaining contribution (91.2%) from calcite. Aqueous Ca complexes corresponding to three different modeling cases in Fig. 2d are presented in Table S2. Speciation results for the case considering all three minerals (calcite, dolomite, and gypsum) show that the effect of $CaSO_4$(aq), which can affect the free Ca^{2+} concentration, is negligible. Hence, PHREEQC model results show that (as expected) calcite is the major contributor of Ca in solution, and they uniquely suggest that IOS is primarily suppressing Ca release from this mineral at 3 h. For this reason, the mechanisms of IOS inhibition on calcite were identified for further study.

3.4. Dissolution of calcite

The effects of 500 and 3000 mg/L IOS addition to brine on calcite dissolution were evaluated over 36 h using sieved calcite particles (150–850 μm); results are shown in Fig. 3a. As with Eagle Ford shale, Ca concentrations in brine with only calcite increase during the monitoring period, and an initial rapid rise is followed by a decreasing rate of increase. This is expected because calcite constituent concentrations (i.e., Ca and CO_3^{2-}) in brine are initially very low, and they increase over time. Comparison of Ca concentrations in brine and IOS brine shows that IOS inhibits dissolution of the calcite particles, although differences at 1 and 36 h are not significant (Fig. 3a).

Results from the calcite particles motivated similar measurements on cleaved calcite at 12 h, but over a wider concentration range; results are shown in Fig. 3b. Measured concentrations of Ca decrease with increasing concentration of IOS from 1 mg/L to 50 mg/L (by up to 90% compared to brine only), and then increase as the IOS concentration exceeds the CMC (94 mg/L). The results show for the first time that a surfactant can substantially inhibit calcite dissolution, and that this inhibition is greatest at intermediate surfactant concentrations. Percent surface coverage at each concentration was calculated based on the same approach taken to calculate surface area coverage for Eagle Ford shale (Section 3.2), and values at 1, 10, 50, 500 and 3000 mg/L of IOS are 1.10%, 9.78%, 32.78%, 69.66% and 77.76%, respectively. Interestingly, the minimum area per molecule calculated from the Gibbs equation (20.7 $Å^2$) is in good agreement with that calculated solely from the adsorption isotherm assuming bilayer adsorption (26.2 $Å^2$). Surface coverage calculations using either the minimum area per molecule from the Gibbs equation or the adsorption isotherm predict monolayer coverage is not exceeded, so results showing less inhibition above 50 mg/L were not expected.

The results suggest that above the CMC (i.e., 94 mg/L), the adsorption density decreases with increasing concentration and thus less inhibition occurs. This might be due to aggregation of IOS above the CMC. Several prior works evaluated surfactant sorption using AFM or molecular dynamics (MD); they demonstrated that surfactants do not always form a continuous film (i.e., monolayer or bilayer). That can aggregate to form micelles, hemimicelles and/or rodlike aggregates on various surfaces at elevated concentrations [66–69]. We also determined via AFM that IOS can form micelles or hemimicelles on a calcite surface at 1000 mg/L (10 × CMC). Thus, decreasing adsorption density of IOS with increasing concentration above the CMC appears reasonable.

The pH and total carbonate concentration were also monitored during calcite dissolution and (along with ionic strength) used to calculate ion activities, (i.e., a_{H^+}, $a_{H_2CO_3^*}$, a_{H_2O}, $a_{Ca^{2+}}$, $a_{HCO_3^-}$). These were used with the aforementioned rate constants to determine which terms in Eq. (1) dominate dissolution [32]. At zero and 3 h, $k_3 a_{H_2O}$ dominates (Table S4). For 6 h and greater, values of $k_3 a_{H_2O}$ are similar to or less than $k_4 a_{Ca^{2+}} a_{HCO_3^-}$, indicating precipitation is also possible. The saturation index ($SI = \log[f_0](Q/K_{sp})$) was also calculated at each time point. It is negative up to and including 12 h, and equal to 0 at 36 h, indicating

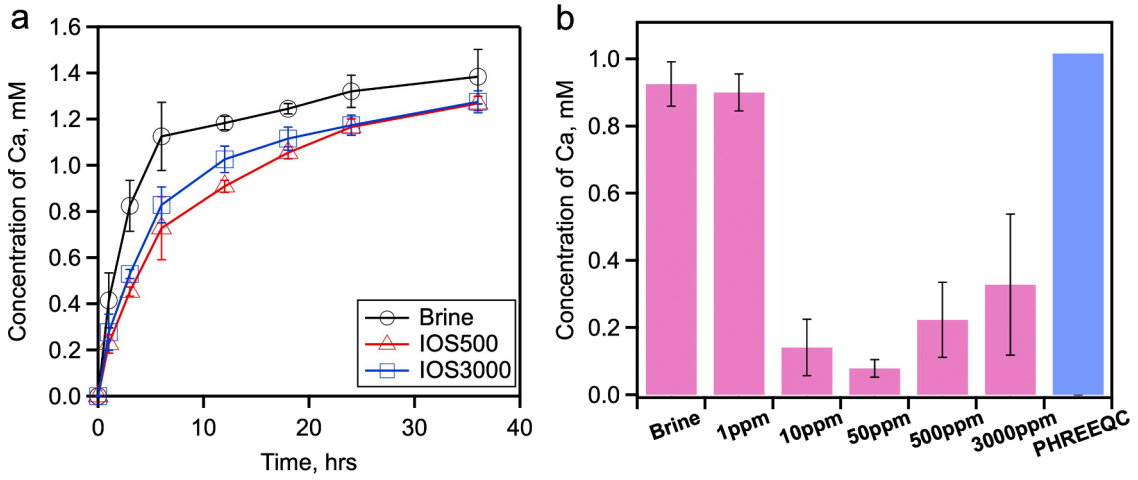

Fig. 3. a) Transient Ca release into solution from calcite particles (150–850 μm) after aging in brine or IOS brine for 36 h. b) Ca release into solution for cleaved calcite piece after aging in brine or IOS brine for 12 h, along with PHREEQC model results showing simulated equilibrium Ca concentration. IOS 500 and IOS 3000 refer to brine with either 500 or 3000 mg/L of IOS added. Initial pH of the solution is 6.3, and ionic strength of brine is 0.4 M. All experiments were run in triplicate, and error bar represents standard deviation.

precipitation is likely after 36 h.

PHREEQC modeling was also performed to determine if the Ca measured in brine solutions during calcite dissolution was near equilibrium. The simulated equilibrium value is approximately 1 mM (Fig. 3b, blue bar). The simulated value is similar to the calcium concentration with cleaved calcite at 12 h (0.95 mM), but below that for calcite particles at 36 h (1.4 mM). The calcite particles after 36 h are likely closer to equilibrium; the reason that the equilibrium Ca value is below the measured value may be due to a small error in the final pH measurement. An error of 0.1 near pH 8 will result in a modeled Ca concentration that is 0.5 mM different.

3.5. Calcite etch pit progression and morphology

Laser profilometry was used to probe etch pit development and identify dissolution mechanisms on freshly cleaved calcite surfaces (i.e., $\{10\bar{1}4\}$ face) placed in brine without and with IOS for 12 h. Results shown in Fig. 4 provide spatial resolution that spans more than three orders of magnitude. In brine only samples, relatively deep and large etch pits are created; etch pit depths are on the order of 5 μm, and etch pit side lengths are approximately 100 μm (Fig. 4a). These etch pits vary in shape from classical rhombohedral to more triangular, where the latter are truncated across the obtuse side of the rhombus along the [010] direction. In IOS brine by contrast, only relatively shallow and small etch pits are created, with depths less than 0.15 μm; also, these etch pits are similar at the two IOS concentrations. Etch pits side lengths are less than 40 μm (Fig. 4b and c). Hence, IOS addition to brine does not prevent initial dissolution but does appear to inhibit etch pit growth.

Cross-sectional profiles across etch pits are also shown in Fig. 4. Etch pit angles were calculated, and are noted in Table 3. In the presence of only brine, the etch pit angle is smaller on the acute side of each rhombus, indicating that pit growth is faster on this edge. This is consistent with faster pit growth at this edge observed in the presence of Mg^{2+} by Arvidson et al. [33]. In the presence of pure water, others observed faster etch pit growth along obtuse edges [70]. In the presence of IOS brine, the shallow and small etch pits formed give rise to very small angles.

Etch pit densities were calculated (i.e., etch pit area divided by total area), and results are presented in Fig. 5b. Surprisingly, a higher fraction of the calcite surface is covered with etch pits for calcite samples in IOS brine compared to only brine. This is also apparent by comparing Fig. 4a with either Fig. 4b or c. These results indicate a contrasting effect, namely that IOS promotes etch pit formation but restricts etch pit growth. These contrasting observations are possible because of the large spatial scale (0.05–200 μm) spanned by laser profilometry.

Table 3
Calcite pit angles.

Angle	Brine		IOS 500		IOS 3000	
	i	ii	iii	iv	v	vi
Pit Angle from Adjacent Horizontal at Acute Edge	6.2°	6.2°	0.5°	0.6°	0.6°	0.7°
Pit Angle from Adjacent Horizontal at Obtuse Edge	53.4°	55.6°	0.8°	0.9°	1.0°	1.9°

In a second set of experiments, calcite surfaces reacted in only brine for 12 h and then dried were re-submerged in either brine or IOS brine for another 12 h. Results are shown in Fig. 6. As expected, etch pits submerged in only brine for the second 12 h continued to grow, and in some cases coalesced. However, etch pits submerged in IOS brine for the second 12 h were almost completely arrested, i.e., they do not appear to have grown further. Examination of the line profiles drawn through etch pits grown in only brine the second 12 h shows that the majority of etch pit growth was along the acute side of each rhombus (blue area in Fig. 6), again indicating preferential growth on this edge.

A surprising result from Fig. 6 is that additional etch pits were not initiated when the sample initially aged in brine only was then aged for another 12 h in IOS brine. From Fig. 4, it is apparent that very high etch pit densities occur when freshly cleaved calcite is initially placed into IOS brine. It is possible that initially formed μm-deep etch pits dominated surfactant sorption and reduce its concentration on flat $\{10\bar{1}4\}$ surfaces, thereby reducing the initiation of new etch pits.

3.6. Preferential adsorption of IOS on calcite etch pits

ToF-SIMS 2D(XY) profiles of SO_2^- for a control sample (calcite aged in

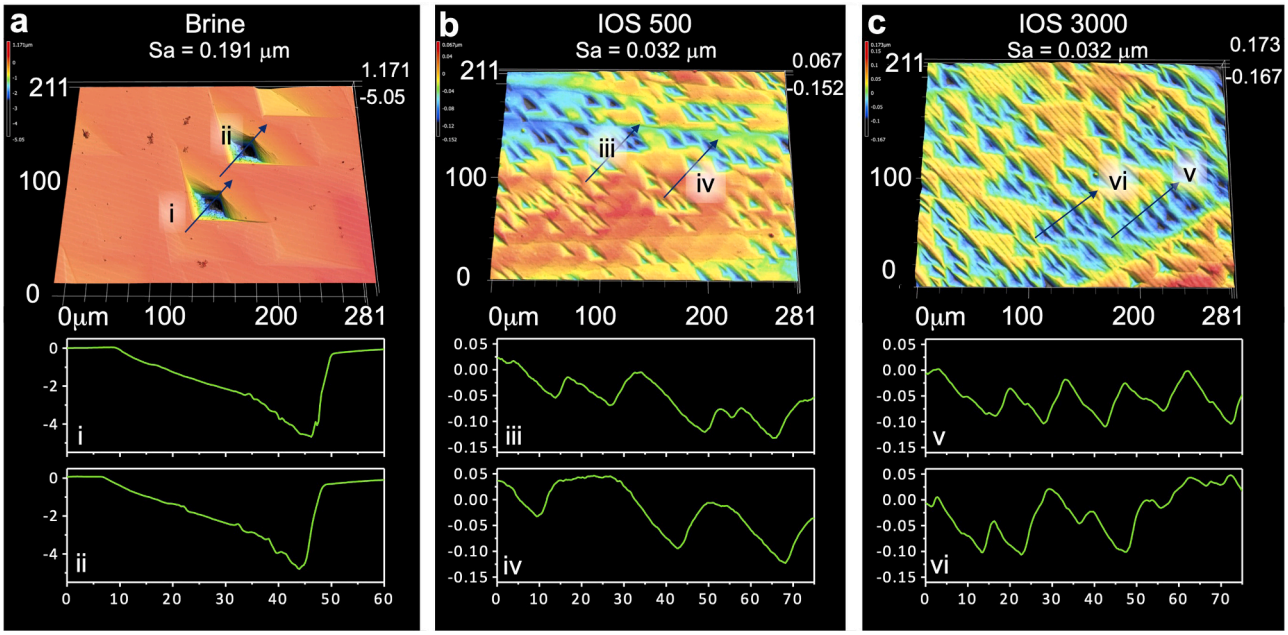

Fig. 4. Laser profilometry results showing etch pits on freshly cleaved calcite surfaces aged in a) brine or b) IOS brine for 12 h. IOS 500 and IOS 3000 refer to brine with either 500 or 3000 mg/L of IOS added. Arithmetic average areal surface roughness (S_a) is provided on top of each surface profile. All the numbers in this figure are in μm.

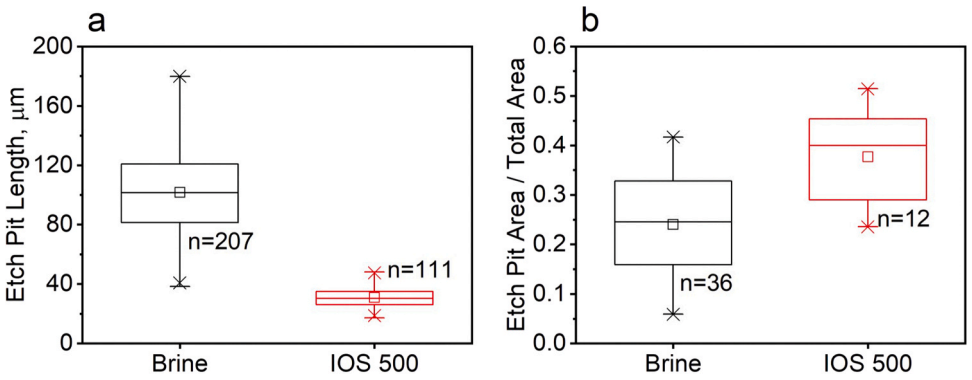

Fig. 5. Box plots showing a) etch pit lengths and b) fraction of calcite surface area occupied by etch pits, both after 12 h of aging in brine without (Brine) or with (IOS 500) IOS surfactant at 500 mg/L. Box plot lines represent median, 25th, and 75th percentile values plus outliers, with mean values shown by a square symbol.

brine) and samples aged in 10 or 100 mg/L IOS (calcite aged in brine and then incubated in IOS) are shown in Fig. 8. The depth profile of SO_2^- in Fig. 7 confirms that with IOS adsorption, SO_2^- accumulates on the top surface of calcite. When no IOS is added to brine, then SO_2^- is not detected on the sample surface (Fig. 8a). At 10 mg/L (0.1 × CMC), IOS appears to preferentially adsorb at acute edges, with distinct areas of high (yellow) and low (brown) coverage (Fig. 8b). While at 100 mg/L, when the concentration is near the CMC, IOS coverage on the surface appears more uniform with intermediate (orange) coverage (Fig. 8c). Preferential IOS adsorption at 10 mg/L to acute edges versus obtuse edges and terrace sites is facilitated by comparison of Fig. 8b to Fig. 8 d, where in the latter the terrace, acute edge, and obtuse edge sites are color coded from the laser profilometry image for ease of comparison with green, red, and blue shades, respectively. Interestingly, surface coverage on the acute edges appears to be denser than that on the obtuse edges. Less dense coverage on the obtuse edge might be due a lower step density at obtuse edges compared to acute edges. A conceptual model of the surface profile along the line indicated by the double arrow in Fig. 8d is presented in Fig. 8e. It is based on the observation that the obtuse edge is much steeper than the acute edge, such that the latter has more steps that preferentially adsorb IOS. This could give rise to more IOS adsorption on the acute versus the obtuse sides of the pit.

Sulfur K-edge NEXAFS spectra of two calibrants (IOS and Gypsum), one control, and four experimental cases are shown in Fig. 9. By decomposing the calibrants (Fig. 9a, b), the energies of the s → p electron transitions of sulfonate and sulfate groups were identified and are approximately 2481($G_{sulfonate}$) and 2482.5 ($G_{sulfate}$) eV, respectively; these are in good agreement with reported values [58]. In addition, sulfate impurities in IOS were also identified ($G_{sulfate,\ IOS}$). The optical quality calcite crystals used in this study originated from nature, so the presence of sulfur impurities (i.e., sulfite, sulfonate, and sulfate) is reasonable (Fig. 9c–e). For example, Pingitore et al. summarized different hypothetical modes of sulfur incorporation into carbonate minerals: i) anhydrite ($CaSO_4$) as mineral inclusions, ii) sulfite (SO_3^{2-}) and sulfate (SO_4^{2-}) substitution for carbonate, iii) sulfate as fluid inclusions, iv) organo-sulfur as organic matter [71]. Also, Perrin et al. experimentally observed the existence of sulfate in their optical quality calcite which contains S below 100 ppm, and sulfite in their synthetic S-MgCalcites using NEXAFS spectroscopy [72].

Due to the uncertainty in the sources of sulfur impurities, we first used three Gaussian functions that represent individual sulfur species with different oxidation states to decompose the spectra. The fractional contributions of three different sulfur functional groups ($G_{sulfite,\ Impr}$, $G_{sulfonate,\ Impr}$, and $G_{sulfate,\ Impr}$) to the measured spectrum were calculated based on the area of Gaussian functions as shown in Fig. 9c. Subsequently, to distinguish the contributions of IOS and sulfur impurities in the prepared samples to sulfonate (2481 eV) and sulfate (2482.5 eV), two Gaussian functions (e.g., $G_{sulfonate,\ IOS}$ (red line) and $G_{sulfonate,\ Impr}$ (blue line)) were used to decompose each functional group contribution (Fig. 9d–g). The ratio between impurities was fixed, assuming that ratios of sulfite to sulfonate and sulfite to sulfate for all calcite samples are identical, since all samples were prepared from one single calcite crystal. Ultimately, areas of $G_{sulfonate,\ IOS}$ (green) in Fig. 9d–g were calculated and summarized in Fig. 9h. Detailed Gaussian-Arctan fitting parameters are in Table S5.

Decomposed sulfur K-edge NEXAFS spectra for each of the IOS adsorbed calcite samples are in good agreement with findings in ToF-SIMS results. The existence of $G_{sulfonate,\ IOS}$, and differences in areas between samples, indicate that SO_2^- detected by ToF-SIMS originates from adsorbed IOS on calcite surfaces. The decomposed NEXAFS spectra enable semiquantitative comparison of the amount of IOS adsorbed on calcite surfaces. Overall, amounts of IOS adsorbed on etched calcite samples were greater than those on unetched (i.e., Not Etched) samples. In agreement with ToF-SIMS results, the NEXASF spectra indicate that IOS preferentially adsorb more to edges compared to terraces on calcite surfaces. Moreover, when samples were exposed to higher concentration of IOS, greater amounts of IOS partitioned onto calcite surfaces (i.e., Fig. 9h Etched 10 vs Etched 100), as observed with ToF-SIMS (Fig. 8a–c).

Calcium K-edge NEXAFS spectra were also measured to probe the effect of IOS adsorption to the surface Ca bonding environment and formation of polymorphs of calcium carbonate. No substantial difference in Ca K-edge NEXAFS spectra was observed between samples (Fig. S2). This might be due to broad spectra peaks or the signal being dominated by bulk calcite. Meanwhile, polymorphs of $CaCO_3$ can form under different thermodynamic conditions and in the presence of surfactants. For example, Chen and Nan reported that precipitation of $CaCO_3$ polymorphs such as aragonite and vaterite can occur in the presence of anionic surfactants [74]. However, as shown in Fig. S2, obtained Ca K-edge NEXAFS spectra of four samples and pristine calcite are similar with no clear signatures of other $CaCO_3$ polymorphs (i.e., amorphous calcium carbonate (ACC), aragonite and vaterite) emerging. Future studies to optimize the surface signal will be helpful to better probe calcite surface chemistry.

Prior efforts to identify preferential adsorption of solutes on edge or terrace sites have relied on less direct measures. Walker et al. treated cleaved calcite with a nonionic surfactant, hexamethyldisilazane (HMDS), to alter calcite wettability. They used Kelvin probe force microscopy (KPFM) to indicate preferential HMDS adsorption at existing step or edge sites [24]. Elhadj et al. and Sand et al. used AFM to image acute and obtuse step edge morphology changes during precipitation in the absence and presence of polyaspartic acid and polysaccharides, respectively [43,75]. They inferred binding location from these measurements, and supported their interpretation with theoretical binding energy calculations. The ToF-SIMS and S K-edge NEXAFS results in this study provide more direct evidence of preferential IOS adsorption at edge sites, thereby suggesting adsorbed IOS is inhibiting dissolution via

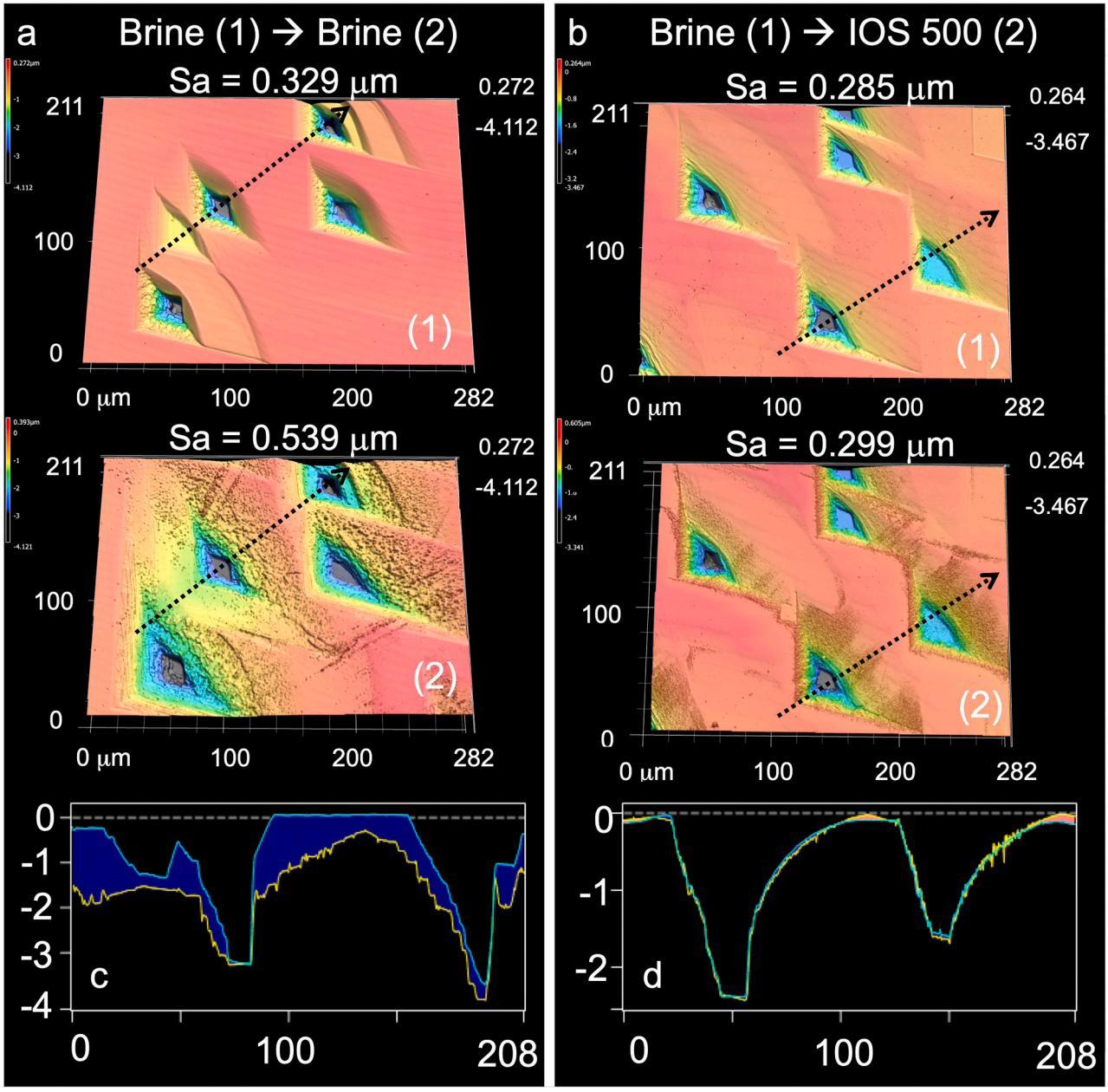

Fig. 6. Laser profilometry results showing etch pits on freshly cleaved calcite surfaces a) aged for two sequential 12 h periods in brine only, and b) aged for two sequential 12 h periods with brine first, and then in IOS brine. IOS 500 refers to brine with 500 mg/L of IOS added. Arithmetic average areal surface roughness (S_a) is provided above each surface profile. All the numbers shown in this figure are in µm.

step pinning at these locations.

3.7. DFT simulation of IOS adsorption on calcite surfaces

In order to better understand the experimental results, DFT was used to calculate binding energies of the IOS molecule on the calcite surface, and binding geometries of the IOS molecule at terrace, acute and obtuse step sites are shown in Fig. 10. The calculated binding energies are shown in Table 4. Our most accurate calculations with implicit solvation indicate that IOS binding is strongest at the acute step (−1.02 eV) site followed closely by the obtuse step (−0.94 eV), and binding at the terrace site (−0.27 eV) is weakest. The same trend was observed for both vacuum and our implicit solvent model, as shown in Table 4. These calculations help to explain how preferential IOS adsorption at both acute and obtuse sites can disrupt and inhibit calcite dissolution. They also support the preferential adsorption of IOS at acute versus obtuse sites as indicated by ToF-SIMS in Section 3.6, and indicate this is at least partially due to preferential adsorption at acute edge versus obtuse edge sites.

3.8. Discussion

Results in this work highlight two apparently opposite effects of the IOS on calcite dissolution. The first is the formation of more etch pits (i.e., higher density) in the presence of IOS (e.g., 12 h, Fig. 3b), and the second is the inhibition of etch pit growth by IOS once they are created. Miyata et al. used MD and DFT to interrogate mechanisms responsible for the growth of etch pits [76]. They simulated dissolution at a calcite edge site, and determined that dissolution starts when adsorbed water dissociates, and the proton is transferred to CO_3 and the hydroxyl ion to Ca. This allows bonds between the proton stabilized CO_3 and Ca to break, creating a separate bicarbonate ion (HCO_3^-) that desorbs from the

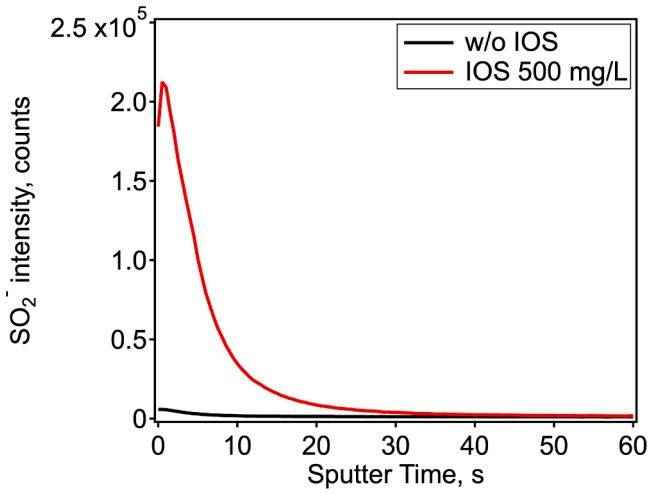

Fig. 7. Background CO_3^- normalized SO_2^- ToF-SIMS profiles of calcite under two different conditions. Solid black line is a sample without IOS, whereas red line is a sample dried after exposure to IOS 500 for 1 h.

calcite edge. The HCO_3^- then decomposes to a hydroxide ion and CO_2, the hydroxide ion adsorbs to Ca, and adsorbed $Ca(OH)_2$ is formed which can desorb into solution. The CO_2 released into solution then forms bicarbonate in bulk water at circumneutral pH. That study highlights the importance of adsorbed water in facilitating Ca and CO_3 hydration at the calcite surface and indicates that solutes that disrupt adsorbed water will affect calcite dissolution.

Nada and Shen et al. determined the binding conformation of aspartic acid and polystyrene sulfonate on a calcite $\{10\bar{1}4\}$ surface using MD [48,77]. First, they showed that three layers of structured water molecules form on the calcite $\{10\bar{1}4\}$ surface. Adsorbed aspartic acid and polystyrene sulfonate are separated from calcite $\left\{10\bar{1}4\right\}$ surface by one or two intervening structured water molecules, and form a weak nonspecific bond with calcite $\left\{10\bar{1}4\right\}$ surface. In addition, Elhadj et al. studied the effect of polyaspartic acid concentration and chain length on calcite crystal growth, and observed growth enhancement at low concentrations and a transition to growth inhibition at high concentrations, where the transition occurred at lower concentrations for larger polyaspartic acids [43]. They attribute the transition to the number of calcite edge sites where polyaspartic acids displace water molecules. At low polyaspartic acid concentrations and low water displacement, sufficient restructuring of water occurs at the calcite surface to reduce the energy for diffusion of solvated ions across this boundary [44]. However, at high polyaspartic acid concentrations and high water displacement, there is sufficient dehydration of contiguous water molecules at the surface that solvation of Ca and CO_3 is inhibited. It follows that the strength and/or amount of IOS adsorption on flat versus edge sites may control contrasting patterns of rapid initial pit formation versus slow pit growth during dissolution.

Surface pressure values calculated from interfacial tensions (Table 2) indicate preferential IOS adsorption to etched versus smooth calcite surfaces, where the former have a higher density of edge sites. ToF-SIMS and S K-edge NEXAFS results support this interpretation, and the former shows IOS preferentially adsorbs to acute versus obtuse and terrace sites. Our DFT results also support this interpretation, and show slightly more favorable IOS adsorption at acute versus obtuse edge sites, both of which are much more favorable than adsorption at terrace sites (i.e., by 0.66–0.74 eV). Similarly, Elhadj et al. found that polyaspartic acids adsorb more strongly to calcite edge versus terrace (flat) sites (by 1.3–6.5 eV) [43]. This leads us to postulate a conceptual model, where oxygen in the sulfonate head group of IOS interacts with Ca at calcite surfaces and displaces water. On calcite terraces, weaker adsorption energies indicates that fewer adsorbed IOS molecules per area displace less water, and they are characterized by faster attachment and detachment rates compared to edge sites. This disruption of water at flat surfaces could lower the energy barrier for diffusion of solvated molecules across the water hydration layer and promote faster pit formation (relative to brine only). However, at edge sites, where more strongly adsorbed IOS molecules are present, IOS molecules displace many more water molecules, and this inhibits CO_3 and Ca solvation and retards pit growth. Our calcite dissolution results with varying IOS concentrations show that as IOS concentrations exceed the CMC calcite dissolution rates increase, and this appears to be caused by IOS aggregation into micelles or hemimicelles on the calcite surface that reduces edge site adsorption coverage.

Surface complexation models (SCMs) for carbonates have been used to explain adsorption isotherms, surface charge, and to model dissolution and growth kinetics when inhibitors are present [78–82]. Defining reactions of surface species and their concentrations significantly affects the accuracy of modeling results. For example, Tagavifar et al. used the diffusion layer model (DLM), which assumes formation of inner sphere complexes, to model surfactant binding to a limestone surface without intervening water molecules [80]. They suggested two different surface reactions were needed based on the surfactant chemical structure: strong adsorption by charge regulated complexation with the surfactant head group; weak adsorption by hydrogen bonding between ethoxy or propoxy groups in the hydrocarbon chain. These proposed complexation reactions were not supported by spectroscopic or computational (i.e., MD and DFT) evidence. However, binding energies from our DFT efforts, as well as ToF-SIM and S K-edge NEXAFS results, support stronger inner sphere complexation of IOS at defect sites (i.e., acute and obtuse edges). They also support weaker complexation at terrace sites, and the exact conformation of IOS at these sites requires further study via DFT and/or spectroscopic evaluation.

4. Conclusions

Primary findings in this work are the following:

- Adsorption of IOS to surfaces of minerals in Eagle Ford shale kinetically inhibited overall release of Ca into bulk solution, and this is attributed to inhibition of calcite dissolution.
- IOS adsorption from brine to calcite both enhances initial etch pit formation, and prevents further etch pit growth.
- ToF-SIMS, S K-edge NEXAFS and DFT results indicate that IOS preferentially adsorbs to edge sites compared to terrace sites.
- The weak binding of IOS to terrace sites observed in this work suggests that enhanced etch pit formation in IOS-containing brines is due to the disruption of structured water molecules at flat surfaces by IOS, resulting in relatively lower energy barriers for diffusion of solvated ions to and from the calcite surface.
- The strong preferential binding of IOS to edge sites suggests that inhibited etch pit growth in IOS-containing brines is due to displacement of water molecules at defect sites (i.e., obtuse and acute edges) by strongly adsorbed IOS molecules, resulting in limited solvation of calcite.

This work shows for the first time how surfactant adsorption amount and location to calcite surfaces can be probed over spatial scales approaching hundreds of microns using optical profilometry coupled with ToF-SIMS and NEXAFS spectroscopy. By comparison, AFM measurements of surfactant adsorption on calcite surfaces are limited to only a few microns. The implications of these results are that surfactants added to slick water, foams, and carbon dioxide injected into shale or conventional formations can inhibit dissolution of carbonate minerals. This may mitigate the formation of preferential flow paths, that could enhance oil and gas recovery from shales, or serve as conduits for upward fluid migration from deep reservoirs to potable groundwater.

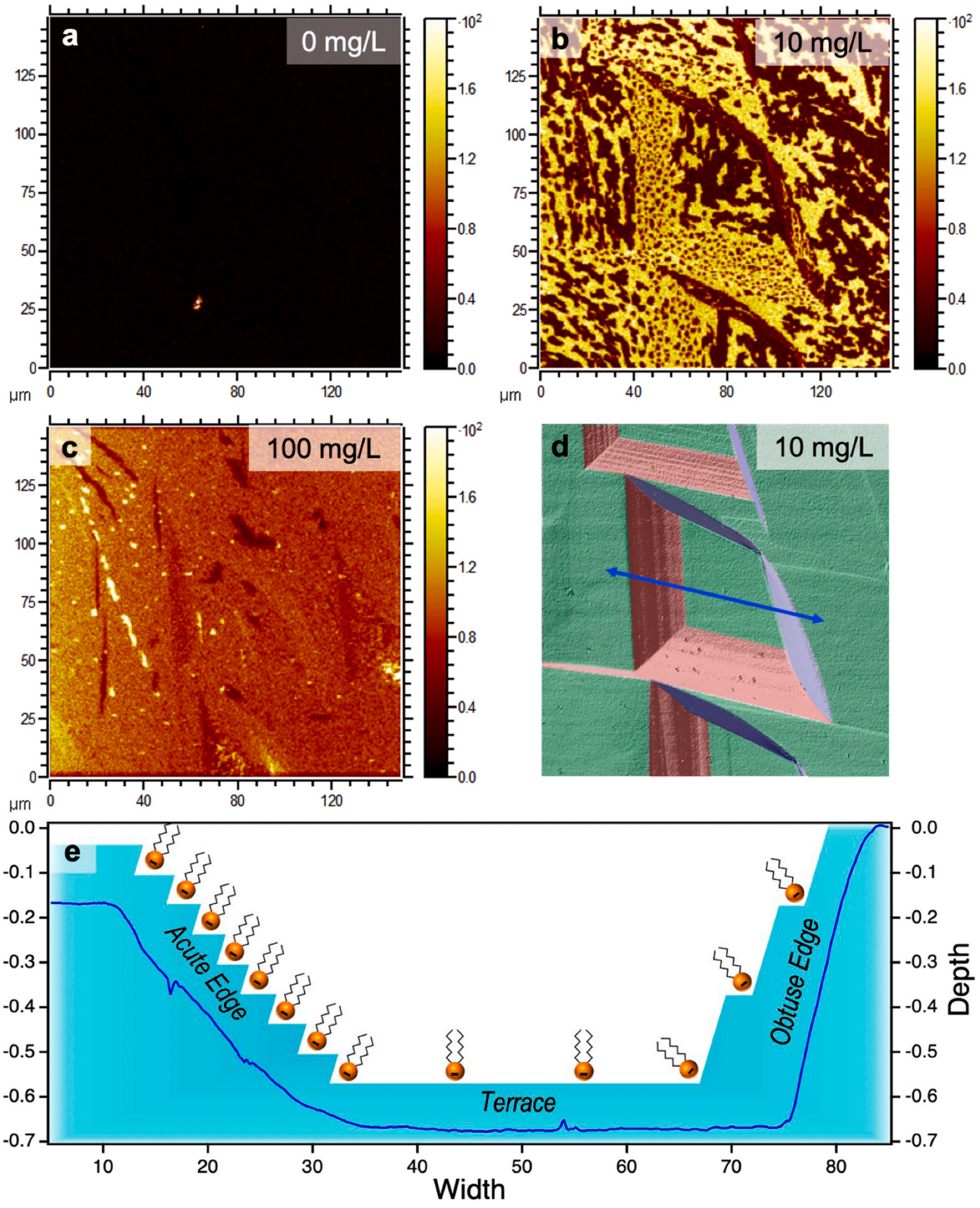

Fig. 8. ToF-SIMS 2D(XY) images of SO_2^- distribution on calcite surfaces after a) aging in only brine for 12 h and then drying, b, c) aging in only brine for 12 h, followed by 10 and 100 mg/L IOS addition, respectively for an additional 1 h, and then drying, d) comparison of laser profilometer result and corresponding b) ToF-SIMS 2D(XY) image of SO_2^-; green, red, and blue shades correspond to terrace, acute edges, and obtuse edges, respectively, e) schematic representation of IOS adsorbed on the calcite surface; surface profile (blue line) shown in e) corresponds to the blue line in d).

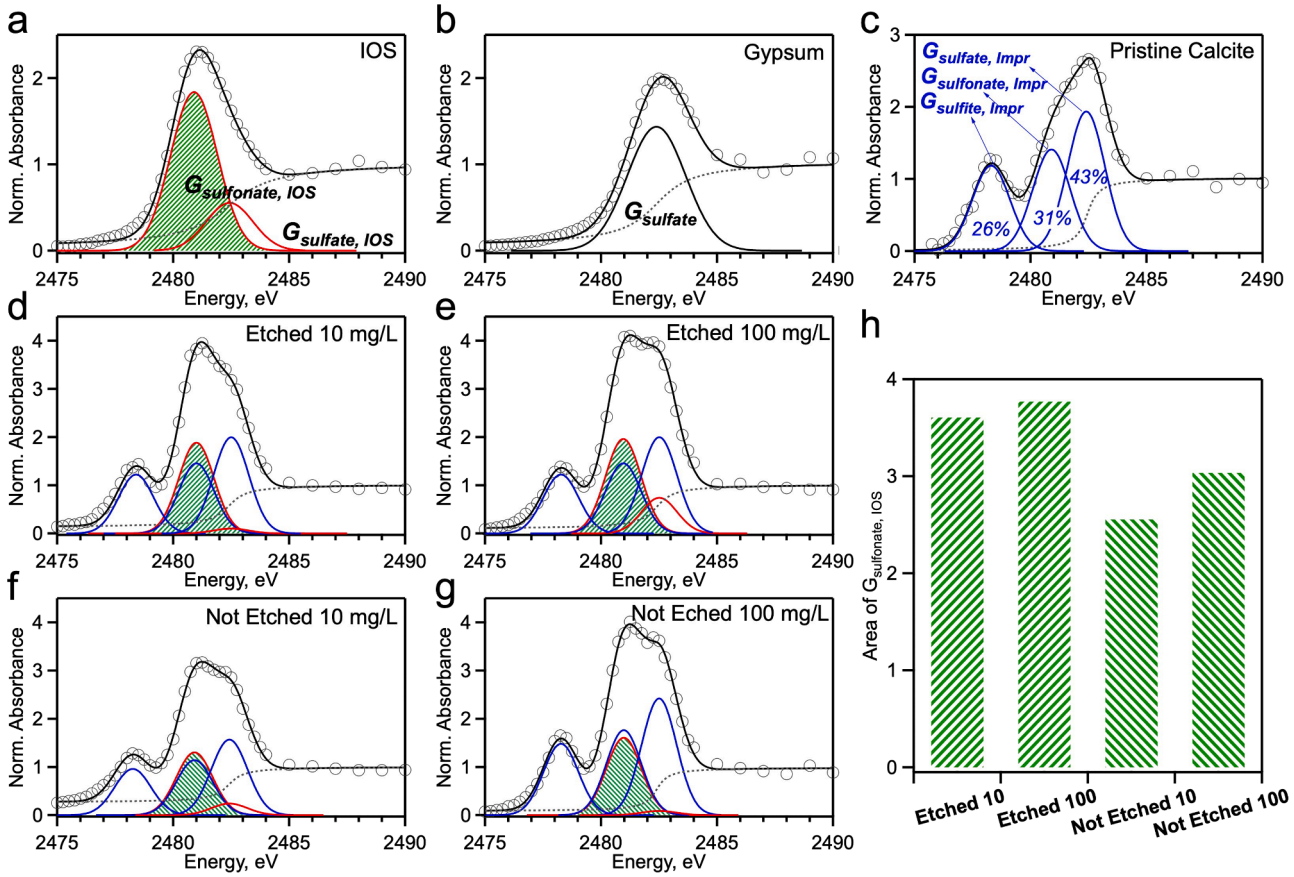

Fig. 9. Sulfur K-edge NEXAFS spectra of: a) A drop of concentrated IOS solution (30.1%) on a silicon wafer. b) Freshly cleaved gypsum without further treatment. c) Freshly cleaved calcite without further treatment. d, e) Freshly cleaved calcite aged in only brine for 12 h, followed by aging for 1 more hour in brine mixed with either 10 and 100 mg/L IOS, and then dried. f, g) Freshly cleaved calcite aged in calcite-saturated brine for 12 h to prevent pit formation, followed by aging for 1 more hour in brine mixed with either 10 and 100 mg/L IOS, and then dried. h) Decomposed peak areas of $G_{sulfonate, IOS}$ (green shaded area of d–g) showing relative amounts of IOS adsorbed to the calcite. Gaussian–Arctan fitting parameters are summarized in Table S5 (Supporting information).

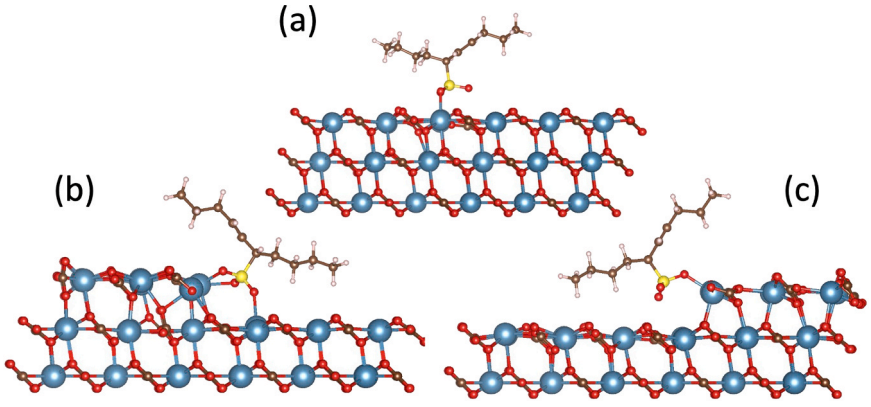

Fig. 10. Side view of IOS adsorption at (a) terrace, (b) acute step and (c) obtuse step sites on the calcite $\{10\bar{1}4\}$ surface.

Table 4
Binding energies of the IOS molecule at different calcite sites.

Binding energies (eV)	Terrace site	Obtuse step	Acute step
Vacuum	−0.78	−2.38	−3.51
Solvent	−0.28	−0.94	−1.02

Further work is needed to determine if the observed effects extend to reservoir pressures and temperatures, and possible implications of these mechanisms in real reservoirs.

CRediT authorship contribution statement

Kyung Tae Kim: Conceptualization, Methodology, Software, Formal analysis, Investigation, Data curation, Visualization, Writing - original draft. **Mantha Sai Pavan Jagannath:** Methodology, Software, Investigation, Visualization, Writing - original draft. **Gregory M. Su**: Methodology, Software, Investigation, Writing - review & editing. **Guillaume Freychet:** Methodology, Investigation, Writing - review & editing. **Tongzhou Zeng:** Conceptualization, Methodology, Formal analysis, Investigation. **Kishore K. Mohanty:** Conceptualization, Methodology,

Resources, Validation, Supervision, Funding acquisition, Writing - review & editing. **Graeme Henkelman:** Conceptualization, Validation, Supervision, Writing - review & editing. **Lynn E. Katz:** Conceptualization, Methodology, Validation, Supervision, Funding acquisition Writing - review & editing. **Charles J. Werth:** Conceptualization, Methodology, Validation, Supervision, Funding acquisition, Writing - original draft, Writing - review & editing, Project administration.

Declaration of Competing Interest

The authors declare that they have no known competing financial interests or personal relationships that could have appeared to influence the work reported in this paper.

Acknowledgments

This material is based upon work supported by the U.S. Department of Energy, Office of Science, Office of Basic Energy Sciences under Award #DE-SC0017328. Spectroscopic investigation of calcite materials was supported as part of the Center for Materials for Water and Energy Systems (M-WET), an Energy Frontier Research Center funded by the U. S. Department of Energy, Office of Science, Basic Energy Sciences under Award #DE-SC0019272. This research used the Soft Matter Interfaces (SMI, Beamline 12-ID) of the National Synchrotron Light Source II, a U. S. Department of Energy (DOE) Office of Science User Facility operated for the DOE Office of Science by Brookhaven National Laboratory under Contract No. DE-SC0012704. The authors thank Dr. Andrei Dolocan (University of Texas at Austin) for assistance with surface characterization using ToF-SIMS.

Appendix A. Supporting information

Supplementary data associated with this article can be found in the online version at doi:10.1016/j.colsurfa.2021.126857.

References

[1] EIA, EIA/ARI World Shale Gas and Shale Oil Resource Assessment Technically Recoverable Shale Gas and Shale Oil Resources: An Assessment of 137 Shale Formations in 41 Countries Outside the United States, 2013. ⟨www.adv-res.com⟩.
[2] EIA, Annual Energy Outlook 2014 with Projections to 2040, 2014. ⟨www.eia.gov/forecasts/aeo⟩.
[3] F. Liu, P. Lu, C. Griffith, S.W. Hedges, Y. Soong, H. Hellevang, C. Zhu, CO_2-brine-caprock interaction: reactivity experiments on Eau Claire shale and a review of relevant literature, Int. J. Greenh. Gas Control 7 (2012) 153–167, https://doi.org/10.1016/j.ijggc.2012.01.012.
[4] M.F. Irfan, T.M. Bisson, E. Bobicki, F. Arguelles-Vivas, Z. Xu, Q. Liu, T. Babadagli, CO_2 storage in saline aquifers by dissolution and residual trapping under supercritical conditions: an experimental investigation, Colloids Surf. A Physicochem. Eng. Asp. 548 (2018) 37–45, https://doi.org/10.1016/j.colsurfa.2018.03.062.
[5] J.A. Chermak, M.E. Schreiber, Mineralogy and trace element geochemistry of gas shales in the United States: environmental implications, Int. J. Coal Geol. 126 (2014) 32–44.
[6] W.C. Dawson, Shale microfacies: Eagle Ford Group (Cenomanian-Turonian) north-central Texas outcrops and subsurface equivalents, Gulf Coast. Assoc. Geol. Soc. Trans. 50 (2000) 607–621.
[7] D.S. Jennings, J. Antia, W.K. Camp, E. Diaz, B. Wawak, Petrographic characterization of the Eagle Ford shale, South Texas: mineralogy, common constituents, and distribution of nanometer-scale pore types. Electron Microscopy of Shale Hydrocarbon Reservoirs, AAPG Memoirs, 2013, pp. 101–113.
[8] J. Schieber, R. Lazar, K. Bohacs, R. Klimentidis, M. Dumitrescu, J. Ottmann, An sem study of porosity in the eagle ford shale of Texas-pore types and porosity distribution in a depositional and sequence-stratigraphic context, AAPG Mem. 110 (2016) 167–186, https://doi.org/10.1306/13541961M1103589.
[9] F. Gherardi, T. Xu, K. Pruess, Numerical modeling of self-limiting and self-enhancing caprock alteration induced by CO_2 storage in a depleted gas reservoir, Chem. Geol. 244 (2007) 103–129.
[10] R. Lahann, M. Mastalerz, J.A. Rupp, A. Drobniak, Influence of CO_2 on New Albany shale composition and pore structure, Int. J. Coal Geol. 108 (2013) 2–9.
[11] J. Rohmer, A. Pluymakers, F. Renard, Mechano-chemical interactions in sedimentary rocks in the context of CO_2 storage: weak acid, weak effects? Earth-Sci. Rev. 157 (2016) 86–110, https://doi.org/10.1016/j.earscirev.2016.03.009.
[12] J.P. Verdon, Significance for secure CO_2 storage of earthquakes induced by fluid injection, Environ. Res. Lett. 9 (2014) 1–10, https://doi.org/10.1088/1748-9326/9/6/064022.
[13] S.A. Carroll, W.W. Mcnab, Z. Dai, S.C. Torres, Reactivity of Mount Simon Sandstone and the Eau Claire shale under CO_2 storage conditions, Environ. Sci. Technol. 47 (2013) 252–261, https://doi.org/10.1021/es301269k.
[14] V. Marcon, C. Joseph, K.E. Carter, S.W. Hedges, C.L. Lopano, G.D. Guthrie, J. A. Hakala, Experimental insights into geochemical changes in hydraulically fractured Marcellus shale, Appl. Geochem. 76 (2017) 36–50.
[16] J.J. Sheng, Status of surfactant EOR technology, Petroleum 1 (2015) 97–105, https://doi.org/10.1016/j.petlm.2015.07.003.
[17] H.C. Tamayo, K.J. Lee, R.S. Taylor, Enhanced aqueous fracturing fluid recovery from tight gas formations: foamed CO_2 pre-pad fracturing fluid and more effective surfactant systems, J. Can. Pet. Technol. 47 (2008) 33–38, https://doi.org/10.2118/08-10-33.
[18] C. Negin, S. Ali, Q. Xie, Most common surfactants employed in chemical enhanced oil recovery, Petroleum 3 (2017) 197–211, https://doi.org/10.1016/j.petlm.2016.11.007.
[19] S. Paria, K.C. Khilar, A review on experimental studies of surfactant adsorption at the hydrophilic solid-water interface, Adv. Colloid Interface Sci. 110 (2004) 75–95, https://doi.org/10.1016/j.cis.2004.03.001.
[20] B. Li, E. Ruckenstein, Adsorption of ionic surfactants on charged solid surfaces from aqueous solutions, Langmuir 12 (1996) 5052–5063.
[21] P. Somasundaran, G.E. Agar, The zero point of charge of calcite, J. Colloid Interface Sci. 24 (1967) 433–440, https://doi.org/10.1016/0021-9797(67)90241-X.
[22] T. Ahmadall, M.V. Gonzalez, J.H. Harwell, J.F. Scamehorn, Reducing surfactant adsorption in carbonate reservoirs, SPE Reserv. Eng. 8 (1993) 117–122, https://doi.org/10.2118/24105-PA.
[23] J.F. Scamehorn, R.S. Schechter, W.H. Wade, Adsorption of surfactants on mineral oxide surfaces from aqueous solutions. I: Isomerically pure anionic surfactants, J. Colloid Interface Sci. 85 (1982) 463–478, https://doi.org/10.1016/0021-9797(82)90013-3.
[24] S.M. Walker, M.C. Marcano, S. Kim, S.D. Taylor, U. Becker, Understanding calcite wettability alteration through surface potential measurements and molecular simulations, J. Phys. Chem. C 121 (2017) 28017–28030, https://doi.org/10.1021/acs.jpcc.7b09565.
[25] H.M. Abd El-Lateef, V.M. Abbasov, L.I. Aliyeva, E.E. Qasimov, I.T. Ismayilov, Inhibition of carbon steel corrosion in CO_2-saturated brine using some newly surfactants based on palm oil: experimental and theoretical investigations, Mater. Chem. Phys. 142 (2013) 502–512, https://doi.org/10.1016/j.matchemphys.2013.07.044.
[26] U. Wehrmeister, D.E. Jacob, A.L. Soldati, N. Loges, T. Häger, W. Hofmeister, Amorphous, nanocrystalline and crystalline calcium carbonates in biological materials, J. Raman Spectrosc. 42 (2011) 926–935, https://doi.org/10.1002/jrs.2835.
[27] T. Matschei, B. Lothenbach, F.P. Glasser, The role of calcium carbonate in cement hydration, Cem. Concr. Res. 37 (2007) 551–558, https://doi.org/10.1016/j.cemconres.2006.10.013.
[28] N.H. De Leeuw, S.C. Parker, J.H. Harding, Self-motion in glass-forming polymers: a molecular dynamics study, Phys. Rev. E Stat. Phys. Plasmas Fluids Relat. Interdiscip. Top. 60 (1999) 6942–6950.
[29] I.N. MacInnis, S.L. Brantley, The role of dislocations and surface morphology in calcite dissolution, Geochim. Cosmochim. Acta 56 (1992) 1113–1126, https://doi.org/10.1016/0016-7037(92)90049-O.
[30] C.A. Orme, A. Noy, A. Wierzbicki, M.T. Mcbride, M. Grantham, H.H. Teng, P. M. Dove, J.J. Deyoreo, Formation of chiral morphologies through selective binding of amino acids to calcite surface steps, Nature 411 (2001) 775–779, https://doi.org/10.1038/35081034.
[31] W. Stumm, Reactivity at the mineral-water interface: dissolution and inhibition, Colloids Surf. A Physicochem. Eng. Asp. 120 (1997) 143–166, https://doi.org/10.1016/S0927-7757(96)03866-6.
[32] L.N. Plummer, T.M.L. Wigley, D.L. Parkhurst, The kinetics of calcite dissolution in CO_2-water systems at 5 degrees to 60 degrees C and 0.0 to 1.0 atm CO_2, Am. J. Sci. 278 (1978) 179–216, https://doi.org/10.2475/ajs.278.2.179.
[33] R.S. Arvidson, M. Collier, K.J. Davis, M.D. Vinson, J.E. Amonette, A. Luttge, Magnesium inhibition of calcite dissolution kinetics, Geochim. Cosmochim. Acta 70 (2006) 583–594.
[34] D.W. Britt, V. Hlady, In-situ atomic force microscope imaging of calcite etch pit morphology changes in undersaturated and 1-hydroxyethylidene-1, 1-diphosphonic acid poisoned solutions, Langmuir 13 (1997) 1873–1876.
[35] R.G. Compton, C.A. Brown, The inhibition of calcite dissolution/precipitation: 1, 2-dicarboxylic acids, J. Colloid Interface Sci. 170 (1995) 586–590.
[36] N.H. De Leeuw, Molecular dynamics simulations of the growth inhibiting effect of Fe2+, Mg2+, Cd2+, and Sr2+ on calcite crystal growth, J. Phys. Chem. B 106 (2002) 5241–5249.
[37] P.M. Dove, M.F. Hochella Jr., Calcite precipitation mechanisms and inhibition by orthophosphate: in situ observations by scanning force microscopy, Geochim. Cosmochim. Acta 57 (1993) 705–714.
[38] C.N. Fredd, H.S. Fogler, The influence of chelating agents on the kinetics of calcite dissolution, J. Colloid Interface Sci. 204 (1998) 187–197.
[39] A.R. Hoch, M.M. Reddy, G.R. Aiken, Calcite crystal growth inhibition by humic substances with emphasis on hydrophobic acids from the Florida Everglades, Geochim. Cosmochim. Acta 64 (2000) 61–72.
[40] M. Ricci, J.J. Segura, B.W. Erickson, G. Fantner, F. Stellacci, K. Voïtchovsky, Growth and dissolution of calcite in the presence of adsorbed stearic acid, Langmuir 31 (2015) 7563–7571, https://doi.org/10.1021/acs.langmuir.5b01732.

[41] E. Ruiz-Agudo, M. Urosevic, C.V. Putnis, C. Rodríguez-Navarro, C. Cardell, A. Putnis, Ion-specific effects on the kinetics of mineral dissolution, Chem. Geol. 281 (2011) 364–371, https://doi.org/10.1016/j.chemgeo.2011.01.003.
[42] T. Yang, W. Huh, J.Y. Jho, I.W. Kim, Effects of fluoride and polymeric additives on the dissolution of calcite and the subsequent formation of fluorite, Colloids Surf. A Physicochem. Eng. Asp. 451 (2014) 75–84, https://doi.org/10.1016/j.colsurfa.2014.03.040.
[43] S. Elhadj, E.A. Salter, A. Wierzbicki, J.J. De Yoreo, N. Han, P.M. Dove, Peptide controls on calcite mineralization: polyaspartate chain length affects growth kinetics and acts as a stereochemical switch on morphology, Cryst. Growth Des. 6 (2006) 197–201.
[44] S. Elhadj, J.J. De Yoreo, J.R. Hoyer, P.M. Dove, Role of molecular charge and hydrophilicity in regulating the kinetics of crystal growth, Proc. Natl. Acad. Sci. 103 (2006) 19237–19242.
[45] K.J. Davis, P.M. Dove, J.J. De Yoreo, The role of Mg2+ as an impurity in calcite growth, Science 290 (2000) 1134–1137.
[46] E. Ruiz-Agudo, M. Kowacz, C.V. Putnis, A. Putnis, The role of background electrolytes on the kinetics and mechanism of calcite dissolution, Geochim. Cosmochim. Acta 74 (2010) 1256–1267, https://doi.org/10.1016/j.gca.2009.11.004.
[47] H.H. Teng, P.M. Dove, Surface site-specific interactions of aspartate with calcite during dissolution: implications for biomineralization, Am. Mineral. 82 (1997) 878–887, https://doi.org/10.2138/am-1997-9-1005.
[48] H. Nada, Difference in the conformation and dynamics of aspartic acid on the flat regions, step edges, and kinks of a calcite surface: a molecular dynamics study, J. Phys. Chem. C 118 (2014) 14335–14345, https://doi.org/10.1021/jp502332c.
[49] I. Choi, I.W. Kim, Purification and partial characterization of a low molecular fibrinolytic serine metalloprotease C142 from the culture supernatant of Bacillus subtilis C142, Int. J. Biol. Macromol. 104 (2017) 724–731, https://doi.org/10.1155/2017/7594950.
[50] J.P. Nicot, A. Gherabati, R. Darvari, P. Mickler, Salinity reversal and water freshening in the Eagle Ford shale, Texas, USA, ACS Earth Space Chem. 2 (2018) 1087–1094, https://doi.org/10.1021/acsearthspacechem.8b00095.
[51] J.R. Barnes, H. Dirkzwager, J.R. Smit, J.P. Smit, R.C. Navarrete, B.H. Ellison, M.A. Buijse, Application of internal olefin sulfonates and other surfactants to EOR. Part 1: Structure – performance relationships for selection at different reservoir conditions, in: Proceedings of the SPE – DOE Symposium on Improved Oil Recovery, OnePetro, 2010, pp. 663–678. ⟨https://doi.org/10.2118/129766-ms⟩.
[52] H. Abdulelah, S. Mahmood, S. Al-Hajri, M. Hakimi, E. Padmanabhan, Retention of hydraulic fracturing water in shale: the influence of anionic surfactant, Energies 11 (2018) 3342, https://doi.org/10.3390/en11123342.
[53] M. Salehi, S.J. Johnson, J.T. Liang, Mechanistic study of wettability alteration using surfactants with applications in naturally fractured reservoirs, Langmuir 24 (2008) 14099–14107, https://doi.org/10.1021/la802464u.
[54] H.H. Teng, Controls by saturation state on etch pit formation during calcite dissolution, Geochim. Cosmochim. Acta 68 (2004) 253–262, https://doi.org/10.1016/S0016-7037(03)00423-X.
[55] C. Amrhein, D.L. Suarez, Procedure for determining sodium-calcium selectivity in calcareous and gypsiferous soils, Soil Sci. Soc. Am. J. 54 (1990) 999–1007, https://doi.org/10.2136/sssaj1990.03615995005400040011x.
[56] E. Costa, D. Aquilano, Experimental value of the specific surface energy of the cleavage {10.4} calcite rhombohedron in the presence of its saturated aqueous solution, Crystals 8 (2018) 1–8, https://doi.org/10.3390/cryst8060238.
[57] X. Hong, M. Newville, T.S. Duffy, High-pressure X-ray absorption fine structure in the diamond anvil cell and its applications in geological materials, J. Phys. Conf. Ser. 430 (2013), 012120, https://doi.org/10.1088/1742-6596/430/1/012007.
[58] A. Manceau, K.L. Nagy, Quantitative analysis of sulfur functional groups in natural organic matter by XANES spectroscopy, Geochim. Cosmochim. Acta 99 (2012) 206–223, https://doi.org/10.1016/j.gca.2012.09.033.
[59] D.L. Parkhurst, C.A.J. Appelo, Description of Input and Examples for PHREEQC Version 3 — A Computer Program For Speciation, Batch-Reaction, One-Dimensional Transport, and Inverse Geochemical Calculations, 2013. ⟨https://doi.org/10.1016/0029-6554(94)90020-5⟩.
[60] A.W. Adamson, A.P. Gast. Physical Chemistry of Surfaces, 5th ed., Interscience, New York, 1990.
[61] J. Botto, S.J. Fuchs, B.W. Fouke, A.F. Clarens, J.T. Freiburg, P.M. Berger, C. J. Werth, Effects of mineral surface properties on supercritical CO_2 wettability in a siliciclastic reservoir, Energy Fuels 31 (2017) 5275–5285, https://doi.org/10.1021/acs.energyfuels.6b03336.
[62] J. Drelich, J.D. Miller, The effect of solid surface heterogeneity and roughness on the contact angle/drop (bubble) size relationship, J. Colloid Interface Sci. 164 (1994) 252–259.
[63] F.M. Fowkes, W.D. Harkins, The state of monolayers adsorbed at the interface solid—aqueous solution, J. Am. Chem. Soc. 62 (1940) 3377–3386.
[64] T. Zeng, K.T. Kim, C.J. Werth, L.E. Katz, K.K. Mohanty, Surfactant adsorption on shale samples: experiments and an additive model, Energy Fuels 34 (2020) 5436–5443, https://doi.org/10.1021/acs.energyfuels.9b04016.
[65] M.J. Rosen, J.T. Kunjappu, Surfactants and Interfacial Phenomena, John Wiley & Sons, 2012.
[66] W.A. Ducker, E.J. Wanless, Surface-aggregate shape transformation, Langmuir 12 (1996) 5915–5920, https://doi.org/10.1021/la9605448.
[67] E.J. Wanless, T.W. Davey, W.A. Ducker, Surface aggregate phase transition, Langmuir 13 (1997) 4223–4228, https://doi.org/10.1021/la970146k.
[68] R.E. Lamont, W.A. Ducker, Surface-induced transformations for surfactant aggregates, J. Am. Chem. Soc. 120 (1998) 7602–7607, https://doi.org/10.1021/ja9742895.
[69] F. Jiménezjiménez-Á Ngeles, A. Khoshnood, A. Firoozabadi, Molecular dynamics simulation of the adsorption and aggregation of ionic surfactants at liquid−solid interfaces, J. Phys. Chem. C (2017), https://doi.org/10.1021/acs.jpcc.7b09466.
[70] A.S. Lea, J.E. Amonette, D.R. Baer, Y. Liang, N.G. Colton, Microscopic effects of carbonate, manganese, and strontium ions on calcite dissolution, Geochim. Cosmochim. Acta 65 (2001) 369–379.
[71] N.E. Pingitore, G. Meitzner, K.M. Love, Identification of sulfate in natural carbonates by X-ray absorption spectroscopy, Geochim. Cosmochim. Acta 59 (1995) 2477–2483, https://doi.org/10.1016/0016-7037(95)00142-5.
[72] J. Perrin, C. Rivard, D. Vielzeuf, D. Laporte, C. Fonquernie, A. Ricolleau, M. Cotte, N. Floquet, The coordination of sulfur in synthetic and biogenic Mg calcites: the red coral case, Geochim. Cosmochim. Acta 197 (2017) 226–244, https://doi.org/10.1016/j.gca.2016.10.017.
[74] Z. Chen, Z. Nan, Controlling the polymorph and morphology of CaCO3 crystals using surfactant mixtures, J. Colloid Interface Sci. 358 (2011) 416–422, https://doi.org/10.1016/j.jcis.2011.02.062.
[75] K.K. Sand, C.S. Pedersen, S. Sjöberg, J.W. Nielsen, E. Makovicky, S.L.S. Stipp, Biomineralization: long-term effectiveness of polysaccharides on the growth and dissolution of calcite, Cryst. Growth Des. 14 (2014) 5486–5494, https://doi.org/10.1021/cg5006743.
[76] K. Miyata, J. Tracey, K. Miyazawa, V. Haapasilta, P. Spijker, Y. Kawagoe, A. S. Foster, K. Tsukamoto, T. Fukuma, Dissolution processes at step edges of calcite in water investigated by high-speed frequency modulation atomic force microscopy and simulation, Nano Lett. 17 (2017) 4083–4089, https://doi.org/10.1021/acs.nanolett.7b00757.
[77] J.-W. Shen, C. Li, N.F.A. Van Der Vegt, C. Peter, Understanding the control of mineralization by polyelectrolyte additives: simulation of preferential binding to calcite surfaces, J. Phys. Chem. C (2013), https://doi.org/10.1021/jp402341w.
[78] P. Van Cappellen, L. Charlet, W. Stumm, P. Wersin, A surface complexation model of the carbonate mineral-aqueous solution interface, Geochim. Cosmochim. Acta 57 (1993) 3505–3518, https://doi.org/10.1016/0016-7037(93)90135-J.
[79] J. Song, S. Rezaee, L. Zhang, Z. Zhang, M. Puerto, O.B. Wani, F. Vargas, S. Alhassan, S.L. Biswal, G.J. Hirasaki, Characterizing the influence of organic carboxylic acids and inorganic silica impurities on the surface charge of natural carbonates using an extended surface complexation model, Energy Fuels (2019), https://doi.org/10.1021/acs.energyfuels.8b03896.
[80] M. Tagavifar, S.H. Jang, H. Sharma, D. Wang, L.Y. Chang, K. Mohanty, G.A. Pope, Effect of pH on adsorption of anionic surfactants on limestone: experimental study and surface complexation modeling, Colloids Surf. A Physicochem. Eng. Asp. 538 (2018) 549–558, https://doi.org/10.1016/j.colsurfa.2017.11.050.
[81] C. Geffroy, A. Foissy, J. Persello, B. Cabane, Surface complexation of calcite by carboxylates in water, J. Colloid Interface Sci. 211 (1999) 45–53, https://doi.org/10.1006/jcis.1998.5966.
[82] O.S. Pokrovsky, J. Schott, Processes at the magnesium-bearing carbonates/solution interface. II. Kinetics and mechanism of magnesite dissolution, Geochim. Cosmochim. Acta 63 (1999) 881–897, https://doi.org/10.1016/S0016-7037(99)00013-7.
[83] M. Bruno, F.R. Massaro, L. Pastero, E. Costa, M. Rubbo, M. Prencipe, D. Aquilano, New estimates of the free energy of calcite/water interfaces for evaluating the equilibrium shape and nucleation mechanisms, Cryst. Growth Des. 13 (2013) 1170–1179, https://doi.org/10.1021/cg3015817.